Front. Optoelectron. 2021, 14(1): 64–93
https://doi.org/10.1007/s12200-020-1081-4

REVIEW ARTICLE

Intense terahertz generation from photoconductive antennas

Elchin ISGANDAROV[1], Xavier ROPAGNOL[1,2], Mangaljit SINGH[1], Tsuneyuki OZAKI (✉)[1]

1 Institut National de la Recherche Scientifique, Centre Énergie, Matériaux Télécommunications (INRS-EMT), Varennes, Québec J3X 1S2, Canada
2 Département de Génie Électrique, École de Technologie Supérieure (ETS), Montréal, Québec H3C 1K3, Canada

Abstract In this paper, we review the past and recent works on generating intense terahertz (THz) pulses from photoconductive antennas (PCAs). We will focus on two types of large-aperture photoconductive antenna (LAPCA) that can generate high-intensity THz pulses (a) those with large-aperture dipoles and (b) those with interdigitated electrodes. We will first describe the principles of THz generation from PCAs. The critical parameters for improving the peak intensity of THz radiation from LAPCAs are summarized. We will then describe the saturation and limitation process of LAPCAs along with the advantages and disadvantages of working with wide-bandgap semiconductor substrates. Then, we will explain the evolution of LAPCA with interdigitated electrodes, which allows one to reduce the photoconductive gap size, and thus obtain higher bias fields while applying lower voltages. We will also describe recent achievements in intense THz pulses generated by interdigitated LAPCAs based on wide-bandgap semiconductors driven by amplified lasers. Finally, we will discuss the future perspectives of THz pulse generation using LAPCAs.

Keywords sub-cycle intense terahertz (THz) pulses, ultrafast Ti:sapphire lasers, wide-bandgap semiconductors, large-aperture photoconductive antenna (LAPCA), phase mask, interdigitated large-aperture photoconductive emitters (ILAPCA)

1 Introduction

The science and technology of terahertz (THz) electromagnetic radiation (with frequencies from 0.1 to 10 THz), located between infrared waves and microwaves, have witnessed significant advances over the past 30 years. For most of the 20th century, research in this part of the electromagnetic spectrum was modest due to the lack of tunable high-power sources and fast, sensitive detectors, thus being dubbed the THz gap [1,2]. Today, we now count numerous techniques for THz generation, such as the synchrotron, free-electron laser, back-wave oscillator, quantum cascade laser, CMOS technology and the laser-based THz sources. In this paper, we will focus on reviewing the principles and the evolution of intense THz sources based on the photoconductive antenna (PCA) emitter, which belongs to the laser-based THz sources.

Intense electromagnetic pulses in the THz frequency range can interact with solids and molecules, thus resulting in excitations at their resonant frequencies. To this end, using high-intensity THz pulses, a series of intriguing scientific studies based on light-matter interaction has recently been performed, including the lattices dynamics (phonons) of crystals, the control of the vibrational-rotational resonance states of molecules, as well as the demonstration of Higgs amplitude mode in Bardeen-Cooper–Schrieffer (BCS) superconductors and Josephson plasmon in layered superconductors [3–12]. The development of pulsed THz radiation from PCAs coincides with the development of ultrafast lasers, and especially the Ti:sapphire laser, which can generate femtosecond light pulses. It was only in 1984 that free-space pulsed THz generation and detection using the PCA was demonstrated [13]. In these studies, two identical antennas with coplanar strip lines with a 10 μm gap size were fabricated on a Si-on-sapphire (SOS) substrate and placed in front of each other. A mode-locked ring dye laser with pulse energy and duration of 50 pJ and 100 fs, respectively, at a repetition rate of 100 MHz was used for pumping the PCA emitter and detector to generate and detect the THz waves. The temporal duration of the detected far-infrared radiation was estimated to be 1.6 ps full-width at half maximum (FWHM). Since then, there have been numerous demonstrations of THz generation, detection and application using PCAs. PCAs are attractive THz sources because they can operate at room temperature without cryogenic cooling. They are very compact and can display high optical-to-THz conversion efficiency while being pumped

Received August 7, 2020; accepted October 16, 2020

E-mail: ozaki@emt.inrs.ca

with relatively low optical power and can generate sub-cycle pulses with relatively high peak powers.

The principle of THz generation from PCA can be described by the current-surge model [14]. A femtosecond laser pulse illuminates a semiconductor crystal, on which the metallic electrodes have been deposited, and a bias voltage is applied. Photons are absorbed by the substrate, exciting carriers from the valence band to the conduction band. These free carriers are then accelerated by the bias field, generating a photocurrent. The variations in photocurrent density, which are in the picosecond time scale, results in the generation of pulsed electromagnetic waves in reflection and transmission direction of the PCA, which are in the THz frequency range. The relationship between the time-dependent photocurrent $J(t)$ and the radiated near field E_{near} is [14]

$$J(t) = \frac{(1+\sqrt{\varepsilon_{\text{r}}})}{\eta_0} E_{\text{near}}(t). \tag{1}$$

Here, η_0 is the free impedance and ε_{r} is the material's relative permittivity. From Ohm's law, $J(t)$ can also be expressed as [15]

$$J(t) = \sigma_{\text{s}}(t)\Big(E_{\text{b}} + E_{\text{near}}(t)\Big). \tag{2}$$

Here, $\sigma_{\text{s}}(t)$ is the surface conductivity of the large-aperture photoconductive antenna (LAPCA), and E_{b} is the bias electric field. The conductivity is proportional to the hole and electron mobility and density. Here, we approximate by considering only the electron mobility, which is constant over the duration of the rising of the current density. In this case, the surface conductivity can be expressed as

$$\sigma_{\text{s}}(t) = e\mu n(t). \tag{3}$$

Here, e is the electron charge, μ is the electron mobility, and $n(t)$ is the time-dependent electron density. When working with a femtosecond laser pulse, the electron density will increase at the timescale of the femtosecond laser and then decrease at a timescale proportional to the time-carrier recombination. Equation (3) can be rewritten as

$$\sigma_{\text{s}}(t) = \frac{e(1-R)\mu}{h\nu}\int_{-\infty}^{\infty} I_{\text{opt}}(t')\exp\left(\frac{t-t'}{\tau_{\text{c}}}\right)\mathrm{d}t'. \tag{4}$$

Here, R is the reflectivity of the LAPCA substrate at the laser wavelength, $h\nu$ is the photon energy, I_{opt} is the optical intensity, and τ_{c} is the carrier lifetime. By combining Eqs. (1) and (2), we obtain a new expression for the radiated near field, E_{near}:

$$E_{\text{near}}(t) = -E_{\text{b}}\eta_0\frac{\sigma_{\text{s}}(t)}{\sigma_{\text{s}}(t)\eta_0 + (1+\sqrt{\varepsilon_{\text{r}}})}. \tag{5}$$

Equation (5) indicates that the radiated near field, E_{near} is linearly proportional to the bias electric field E_{b}. Further, the scaling of E_{near} is proportional to the surface conductivity but scales hyperbolically. The maximum radiated near field, $E_{\text{near}}^{\text{max}}$, is expressed as

$$E_{\text{near}}^{\text{max}} = -E_{\text{b}}\eta_0\frac{\sigma_{\text{s}}^{\text{max}}}{\sigma_{\text{s}}^{\text{max}}\eta_0 + (1+\sqrt{\varepsilon_{\text{r}}})}. \tag{6}$$

Here, $\sigma_{\text{s}}^{\text{max}}$ is the maximum surface conductivity. In our case, the maximum surface conductivity appears just at the end of the laser pulse before carrier recombination happens. From Eq. (4), the maximum surface conductivity can be express as follows:

$$\sigma_{\text{s}}^{\text{max}} = \frac{e(1-R)\mu F_{\text{opt}}}{h\nu}. \tag{7}$$

Here, F_{opt} is the optical fluence. From Eqs. (6) and (7), the new expression for the radiated near field is

$$E_{\text{near}}^{\text{max}} = -E_{\text{b}}\frac{F_{\text{opt}}}{F_{\text{opt}} + \dfrac{h\nu(1+\sqrt{\varepsilon_{\text{r}}})}{e(1-R)\mu\eta_0}} = -E_{\text{b}}\frac{F_{\text{opt}}}{F_{\text{opt}} + F_{\text{sat}}}. \tag{8}$$

Here, F_{sat} is the saturation fluence and is inversely proportional to the electron mobility.

$$F_{\text{sat}} = \frac{h\nu(1+\sqrt{\varepsilon_{\text{r}}})}{e(1-R)\mu\eta_0}. \tag{9}$$

From Eq. (8), we see that the radiated near field scales hyperbolically with fluence. Consequently, by increasing the optical fluence, we reach a saturation regime, where the radiated near field saturates as a function of the optical fluence (the laser energy). Physically, when the optical fluence is low compared to the saturation fluence, the radiated near field scales almost linearly. In contrast, when the optical fluence is large, the amplitude of the radiated near field saturates. Note that the direction of the radiated near field is in the direction opposite to the bias electric field. Physically, in the latter condition, when the amplitude of the radiated near field is comparable to the amplitude of the bias electric field, it screens the bias electric field itself, which leads to the saturation of the radiated near field. When the LAPCA operates in the screening regime, the only way to increase the amplitude of the radiated near field is to apply a higher bias field. The expression of the radiated far-field is

$$E_{\text{far}}(t) \propto \frac{\partial J}{\partial t} \propto E_{\text{bias}}\frac{\partial n}{\partial t}. \tag{10}$$

The optical-to-THz conversion efficiency of LAPCAs is expressed by [16]

$$\eta = \frac{\tau E_{\text{bias}}^2}{2F_{\text{opt}}\eta_0}\left(\frac{F_{\text{opt}}}{F_{\text{opt}} + F_{\text{sat}}}\right)^2. \tag{11}$$

Here, τ is the duration of the THz pulse. As expected,

the optical-to-THz conversion efficiency scales quadratically with the bias field. The maximum optical-to-THz conversion efficiency is obtained when the optical fluence is equal to the saturation fluence.

$$\eta_{\max} = \frac{\tau E_b^2}{8F_{sat}\eta_0}. \quad (12)$$

The energy of the THz pulses can be expressed as follows:

$$W_{THz} = \eta \times W_{opt} = \eta \times A \times F_{opt}. \quad (13)$$

Here, W_{THz} and W_{opt} are the THz and optical energy, respectively, and A is the area of the optical beam, which we consider to be equal to the illuminated area of the LAPCA. For a specific bias field, the maximum THz energy is given by combining Eqs. (12) and (13):

$$W_{THz}^{max} = \frac{A \times \tau E_b^2}{8\eta_0}. \quad (14)$$

From Eq. (14), we see that the maximum THz energy only depends on the square of the bias field and the area of the LAPCA. Further, as Eq. (14) indicates, the THz energy of a PCA source is extracted from the bias voltage rather than the optical pump power. This characteristic is also particularly advantageous for achieving high optical-to-THz conversion efficiency while using a relatively low optical energy, for example, when using an oscillator laser. This characteristic is unique compared with other THz sources based on nonlinear optical processes, such as optical rectification. Studies on THz generation and detection were significantly bolstered with the advent of femtosecond Ti:sapphire lasers, which is one of the most widely used femtosecond lasers since the 1990s, with a central wavelength at 800 nm and corresponding photon energy of 1.55 eV. To take advantage of the characteristics of the Ti:sapphire laser, PCAs were fabricated and studied using semiconductors with a bandgap smaller than 1.55 eV to optimize the photon absorption and thus the quantum efficiency of the PCA. Due to the fantastic properties for use in PCA, such as relatively high dielectric strength, high carrier mobility and ideal bandgap, GaAs rapidly became the substrate of choice for PCA in the past 20 years. These PCAs became widely used as both THz emitters and detectors, leading to the creation of new functionalities such as THz time-domain spectroscopy (TDS), which was first demonstrated in 1990 by Grischkowsky et al. [17]. THz-TDS differs from Fourier-Transform Infrared spectroscopy in that it measures the time-dependent electric field and phase of the THz pulse [18–22]. Other applications such as imaging, security screening, non-destructive control and telecommunication are also being developed [23–28]. These applications typically use microstructure PCA sources, having a micro pattern that allows much lower bias voltages to be used. In addition, these sources can be pumped by oscillator lasers with nJ-level optical energy and high repetition rate, leading to the emission of THz pulses with high average power and measurements with high dynamic range. Despite requiring microfabrication with a photolithography technique, this microstructure PCA is relatively standard to make and can reach an optical-THz conversion efficiency ranging from 10^{-3} to 10^{-4}. Furthermore, by pushing to the extreme the technology of electrodes, such as nanoisland, nanoantenna and plasmonic electrodes, the photoconductive emitter can generate broadband THz radiation with an optical-to-THz conversion efficiency of 7.5%, which is the highest conversion efficiency recorded to date [29–32]. On the other hand, intense THz pulses (such as LAPCA THz sources) driven by high peak power amplified lasers are opening a new field that studies the nonlinear interactions between matter and intense THz waves. Nonlinear non-resonant effects have been revealed, such as the ionization of Rydberg atoms, absorption bleaching and high-frequency THz generation [33–35]. Indeed, LAPCAs can typically generate asymmetric quasi-half-cycle THz pulses consisting of a large positive peak followed by a long but weak negative tail. The main frequency components of these emitted THz pulses are in the lower part (< 1 THz) of the THz spectrum. These two characteristics are unique from tabletop laser-driven strong-field THz sources [36]. These intense, low-frequency THz pulses with the half cycle of the driving field generate high ponderomotive potential and are ideal for carrier acceleration in solids, which is crucial for initiating nonlinear non-resonant effects in matter. The ponderomotive energy is the cycle-averaged energy of an electron in the THz field, which is expressed as follows [37]:

$$W_p = \frac{eE_{peak}^2}{4m_0\omega^2}. \quad (15)$$

Here, e is the electric charge, E_{peak} is the peak electric field, and m_0 and ω are the effective mass and the angular frequency of the THz electric field, respectively.

In the past 20 years, there has been significant progress in developing THz sources based on PCAs, with considerable improvement in their performances and reliability. In this review paper, we provide an overview of past progress and the state-of-the-art of PCAs, especially for generating intense THz pulses. This review is composed of the following two sections. Section 2 describes the LAPCAs, and Section 3 will talk about the interdigitated large-aperture photoconductive antennas (ILAPCAs). In Section 2, we will describe THz wave generation from conventional LAPCA and discuss their respective performances and limitations. Therefore, in Section 2.2.1, we describe comparative studies on the performances of THz pulse generation from GaAs and ZnSe LAPCAs excited with 800 and 400 nm laser pulses. The performances of 6H-SiC and 4H-SiC LAPCAs excited

with a 400 nm laser pulse are described in Section 2.2.2, and the performances of LAPCAs fabricated from various wide bandgap semiconductor crystals under the illumination of ultraviolet (UV) lasers pulses are described in Section 2.2.3.

Potential photoconductive materials and the main parameters that lead to a substantial increase in the THz power of LAPCAs will also be described in this section. Then, in Section 3, we will describe ILAPCAs and their developments to overcome the limitations in the conventional large-aperture emitters. We will also discuss both past and recent progress in intense THz wave generation from interdigitated photoconductive emitters. A general overview of intense THz wave generation from ILAPCAs and the various techniques used to improve the antenna performance are described in Section 3.1. Furthermore, direct comparative studies of the performances of 6H-SiC and 4H-SiC ILAPCAs under the excitation sub-picosecond UV lasers are given in Sections 3.2 and 3.3, respectively. Finally, we will describe the most recent studies performed on improving the intensity of THz waves from LAPCAs.

2 Terahertz radiation generated from LAPCAs

Photoconductive emitters with large photo-excited surfaces and simple strip-line electrodes are a simple way to improve the peak electric field of THz pulses by increasing the total excited area but keeping the same optical fluence as in conventional PCAs [34,35,38,39]. The typical emitting surface of LAPCAs can vary from hundreds of mm^2 to a few tens of cm^2. The electrode gap size of these emitters is much larger than the wavelength of the emitted THz pulses, with spacing between the electrodes ranging from 1 mm to 1 cm [34,40,41]. Semi-large PCAs have an inter-electrode distance much smaller than the LAPCA, and sometimes the gap size is equivalent to the emitted wavelength ranging from a few hundred μm to 1 mm. However, for semi-large PCA, the theory, described in the introduction, remains the same. The schematic diagram of a conventional LAPCA is shown in Fig. 1. To take full advantage of the large area of these emitters, we need to work with a large laser beam, which in turn requires higher energy. The consequence will be an injection of a larger number of carriers, which results in a larger radiated electric field. Further, unlike micro-dipole photoconductive emitters, LAPCAs do not suffer from the space-charge-field screening effect [42], which is one of the saturation effects limiting the intensity of the THz pulses. The origin of this effect can be explained by the separation of free charges (electron-hole) in the semiconductor. These free carriers are accelerated under the applied bias field, thus generating a static Coulomb field, which is in the opposite direction of the bias field and ultimately causes partial screening of the applied bias fields in the ps timescale [42,43]. Using Monte-Carlo simulations, it was also shown that in GaAs, space charge is almost negligible when the inter-electrode spacing is larger than 100 μm [42]. Studies have shown that the choice of the semiconductor substrate greatly influences the performances of the LAPCAs. Usually, for the generation of high-intensity THz pulses, it is preferable to work with a semiconductor substrate with high dielectric strength, excellent thermal properties and high carrier mobility [35,44–48]. From this perspective, the first intense THz source using a LAPCA was demonstrated by You et al. [39]. In their study, two aluminum electrodes were fabricated on opposite sides of a GaAs substrate with a dimension of 3.5 cm × 3.5 cm. This emitter generated THz pulses with an energy of 0.8 μJ when illuminated with an excitation fluence of 40 $\mu J/cm^2$ and an applied bias field of 10.7 kV/cm. With its calculated peak THz electric field of 150 kV/cm and optical-to-THz conversion efficiency of 1.6×10^{-3}, this source can be considered as one of the most effective LAPCA THz sources to date. Another early demonstration of THz wave generation from low-temperature grown (LT) GaAs LAPCA was performed by Darrow et al. [14]. With a photoconductive gap of 0.5 mm, the antenna was excited by a mode-locked ring dye laser with pulse energy and a duration of 8 μJ and 70 fs, respectively, at a central wavelength of 618 nm. The waveform of radiated THz pulses from the antenna was a quasi-half cycle with a duration of 600 fs FWHM. The scaling of the THz radiated field as a function of the optical excitation fluence was studied with increasing applied bias fields from 1.0 to 4.0 kV/cm (Fig. 2). For high fluence excitations of 1 mJ/cm^2, a strong saturation behavior in the peak amplitude of the THz fields was observed for all values of the applied bias fields. Further, increasing the bias field up to 5 kV/cm caused thermal damage at an optical fluence of

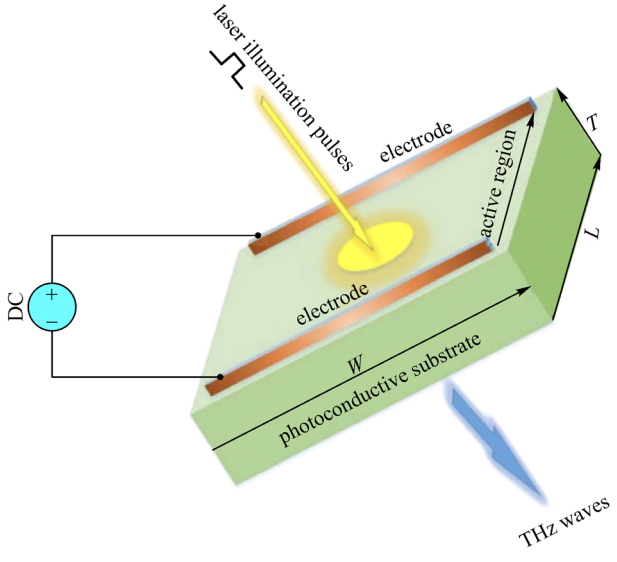

Fig. 1 Schematic view of a typical large-aperture photoconductive emitter [38]

1 mJ/cm^2. Experimental studies performed on the LAPCAs using semi-insulating (SI) GaAs, InP and ZnSe substrates have shown that the screening of the bias field appears for all types of antennas and all bias field when they are excited with a high optical fluence, relative to the saturation fluence, and with photon energy that is higher than the semiconductor bandgap [18,49–51]. From this perspective, we can clearly see that increasing the optical fluence leads to the saturation of the THz field. The advantage of working within the screening regime is that the LAPCA will have less fluctuation in the radiated field. This is especially true when these LAPCA are pumped with an amplified laser with a very low repetition rate. In this case, one way to increase the intensity of the THz pulses is to increase the bias field. A recent theoretical study has shown that an applied external magnetic field parallel to the electrode direction can also be an effective solution to increase the maximum intensity of the THz pulses radiated by LAPCAs [52].

2.1 Parameters that influence the performance of high-intensity THz LAPCAs

Most of the substrates used for fabrications of LAPCAs for the generation of intense THz pulses have some common characteristics such as large dielectric strength, high carrier mobility, and good thermal conductivity. In the following section, we will describe some of the parameters that influence the performance of LAPCAs. Table 1 summarizes the main parameters of several semiconductors that have already been studied as a substrate for LAPCA and THz generation [53].

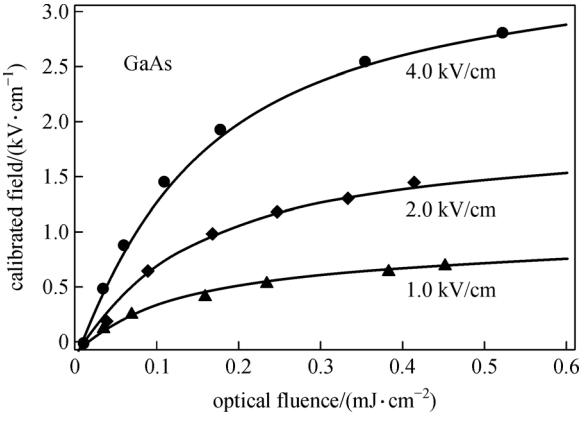

Fig. 2 Calibrated radiated field as a function of optical fluence from a 0.5 mm gap GaAs antenna at bias fields of 4.0, 2.0, and 1.0 kV/cm [13]

2.1.1 Bandgap

The bandgap is presumably the most crucial parameter when selecting a substrate for the fabrication of LAPCAs. Indeed, the bandgap determines which wavelength we can use for THz generation. To strongly enhance the photon absorption, the photon energy of the laser pulse should be slightly higher than the bandgap. This will allow an efficient absorption with high quantum efficiency, but also the free carriers will be generated at the bottom of the conduction band, where the carrier mobility is the highest. Another parameter to take into consideration is the relationship between the bandgap E_G and the dielectric strength E_c. This empiric relationship is expressed by [62]

$$E_c = 1.36 \times 10^7 \left(\frac{E_G}{4}\right)^2. \quad (16)$$

As we can see, a small increase in bandgap energy will induce a large difference in dielectric strength. This is crucial for LAPCA since the radiated peak electric field is linearly proportional to the bias electric field. This simple equation shows the advantage of using a wide bandgap semiconductor crystal for the substrate of LAPCAs. Another parameter that is linked to the bandgap is the dark resistivity. Indeed, the larger the bandgap of a semiconductor is, the smaller the intrinsic carrier concentration is, and the larger the dark resistivity is. Since LAPCAs require high voltage, which is applied mainly during the on-state of the photoconductive switch but also during the off-state if working with a high voltage pulse generator, a high dark resistivity will limit the current leakage induced by the high voltage during the off state of the photoconductive switch, thereby limiting the heating of the LAPCAs. Experimentally, wide-bandgap semiconductors such as diamond, gallium nitride (GaN), zinc selenide (ZnSe), zinc oxide (ZnO) and silicon carbide (SiC) have been tested for THz generation with LAPCAs [35,55,56,

Table 1 Important parameters of semiconductors used for the fabrication of PCAs [47,54–61]

crystal	E_G/eV	E_c/(kV·cm^{-1})	μ/(cm^2·V^{-1}·s^{-1})	τ_c/ps	ρ/(Ω·cm^{-1})	K/(W·cm^{-1}·K^{-1})
SI-GaAs	1.44	<10	9500	2–10	10^6–10^8	0.27
LT-GaAs	1.44	10	150–200	0.3–1	10^6	0.27
diamond	5.46	2000	2800	–	10^{11}–10^{18}	25
GaN	3.40	300	1250	>150	$>10^8$	1.3
ZnSe mono	2.67	60	300–600	>500	10^{12}	0.18
6H-SiC	3.23	>500	200–300	1000	$>10^{12}$	3.7
4H-SiC	3.02	1000	800	<1000	$<10^{12}$	3.7

Notes: E_G, bandgap; E_c, material dielectric strength; μ, carrier mobility; τ_c, carrier lifetime; ρ, resistivity; K, thermal conductivity

61,63]. More details about these experiments will be described below.

2.1.2 Carrier mobility

Carrier mobility is the second main parameter that should be taken into consideration. Indeed, in theory, the carrier mobility does not affect the maximum intensity of THz pulses radiated from LAPCAs, but it will affect the maximum efficiency that we can obtain as expressed in Eq. (12), since the maximum efficiency is linearly proportional to the carrier mobility. Another consequence is that the saturation fluence is higher, thus requiring more optical energy to reach the screening regime. Also, the effects of the relatively low carrier mobility on the THz intensity can be compensated by increasing the energy of the driver laser, allowing more carriers to be injected to achieve the same current density.

Some simulations show that the substrates with higher electron mobility do not exhibit enhancement in the THz intensity [64–66]. Experimentally, it is difficult to have the same substrate with the same characteristics with only a difference in carrier mobility. The closest example we can cite is probably LT-GaAs versus SI-GaAs. The difference in carrier mobility is 200 $cm^2/(V \cdot s)$ versus 8500 $cm^2/(V \cdot s)$. Even though some other parameters (such as the carrier lifetime) also differ, the experimental results are truly intriguing. It was shown that using low optical power or fluence, the SI-GaAs photoconductive emitter was more efficient and radiates a higher THz electric field than the LT-GaAs PCA. However, by increasing the laser energy (power), while the SI-GaAs was already working in the THz screening regime, the electric field radiated by the LT-GaAs PCA increased and was slightly larger [47,67]. Another important parameter to take into consideration is the fact that the mobility of carriers, when injected from the valence band to the conduction band, rarely reached the steady-state, where the mobility of carriers is the highest. For example, it was found that for excitations of 815 nm from a dye amplified laser, the effective carrier mobility was found to be 430 $cm^2/(V \cdot s)$ in SI-GaAs LAPCA [68], which is significantly less than the steady-state carrier mobility of GaAs (8500 $cm^2/(V \cdot s)$). This was attributed to the generation of hot electrons and the electron scattering process.

2.1.3 Carrier recombination time

Carrier recombination is another parameter that influences the performance of PCAs. As we discussed in Section 1, the THz pulses radiated in the far-field is proportional to the time derivative of the photocurrent density induced inside the PCA. Figure 3 illustrates the current density and the intensity profile of the femtosecond optical pulse as a function of time inside a PCA, as well as the temporal profile of the electric field of the THz pulse propagating in the far-field [69]. As can be seen in Fig. 3, in an ideal case, the temporal profile of the photocurrent reaches its maximum value at the end of the optical pulse duration. On the other hand, carrier recombination is the main dominating factor that influences the decay time of photocurrent. The temporal profile of the THz pulses emitted by LAPCAs in the far-field depends on how fast the photocurrent increases and decreases. In this specific illustration, the THz pulses are composed of a positive peak, followed by a long and negative tail. Experimentally, many examples show that the THz waveforms are a quasi-half cycle and exhibit a strong asymmetry.

For THz radiation from LAPCAs, the role of carrier lifetime can be distinguished into two different regimes relative to the duration of the optical pulses [70–72]. In the first case, the carrier lifetime is approximately equal or shorter than the laser pulse duration. The second case is when the carrier lifetime is longer than the optical pulse duration. In the first regime, free carriers start to recombine before or just after the total duration of the laser pulse. Consequently, an extremely rapid decay in photocurrent is observed. Of course, in this configuration, the THz waveforms would not be a quasi-half cycle pulse but will be more a single-cycle pulse with good symmetry between the positive and the negative peak. Numerical studies performed on different semiconductors have shown that when the carrier recombination is faster than 1 ps, the time profile of the radiated electric field has a higher symmetry between the positive and the negative part of the THz pulse [52,71–75]. To put in evidence this phenomenon experimentally, studies performed on LAPCAs made from LT-GaAs with carrier lifetime ranging from 0.35 to 1.2 ps have shown that these substrates exhibit a clear transition in the amplitude of the emitted THz pulses from nearly symmetric bipolar to a quasi-unipolar waveform [67]. In other words, the LAPCA with the shortest carrier lifetime radiates THz pulses with a good symmetry while the one with the 1.2 ps carrier lifetime was strongly asymmetric with a slight enhancement of the THz peak electric field (Figs. 4(a) – 4(c)). The strong negative peak observed in the THz pulses emitted by the shortest carrier lifetime LT-GaAs LAPCAs is due to the faster decay in transient photocurrent occurring because of the relatively short carrier lifetime. In the second regime, where the carrier lifetime is much longer than the duration of the optical pulse, the decay of photocurrent is relatively slow, and then the derivative of this part is almost zero. Thus, the negative polarity of the THz waveform tends to zero. Numerically, it has been shown that a carrier lifetime longer than 2 ps has almost no effect on the peak photocurrent density and the THz waveforms [73–76]. Experimentally, all the LAPCAs fabricated from semiconductors with time carrier lifetime longer than 2 ps generate asymmetric quasi-half-cycle THz pulses [38,67]. There is a significant advantage of having a

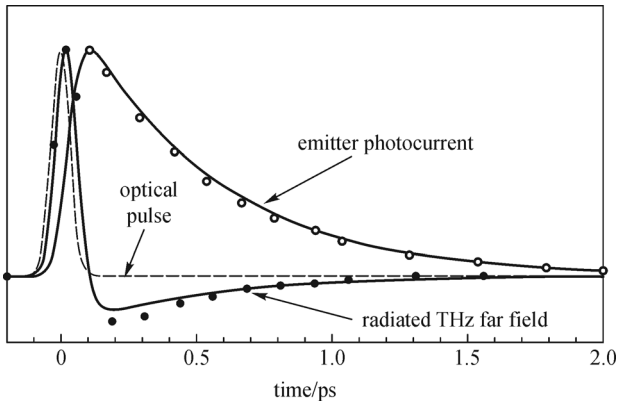

Fig. 3 Calculated photocurrent, the amplitude of the radiated electric field and the laser pulse shape as a function of time [69]

substrate with a short carrier lifetime, for example, below 1 ps, if the maximum radiated peak electric field is not impacted, we could apply a larger bias field. We will discuss this point in the next section.

There have been several theoretical studies on the influence of the laser pulse duration on the THz pulses emitted by photoconductive emitters [69,72,77]. This latter parameter has a great influence since the THz electric field is proportional to the time derivative of the photocurrent density. Intuitively, one could imagine that a longer pulse duration induces a longer time injection of free carriers, which in turn creates a slower current transient and less intense peak current. Consequently, the duration of the half-cycle pulses of the emitted THz pulse will be longer with a smaller peak electric field. Simulations based on the Drude-Lorentz theory model or by a semi-classical Monte-Carlo simulation showed that for a laser pulse duration of 30 fs and above, when the laser pulse duration is increased, the THz peak field decreased, the duration of the THz pulse increases and the frequencies components of this pulse are narrower and the peak frequency shifts toward lower frequency [70,72,77,78]. More surprisingly, the three-dimensional Monte-Carlo simulation shows that the peak of the THz peak field is reached for a laser pulse duration of 40 fs. However, for shorter laser pulse duration, the THz peak field decreases [70]. This drop is attributed to the fact that a shorter laser pulse with a duration below 40 fs is extremely broad. Consequently, the variation of photon energy is also large. For example, photons with energy smaller than the bandgap will not participate in the processes of THz generation since they will not be absorbed by the substrate. In opposition, photons with much larger energy than the bandgap could scatter in the satellite valley where the electron mass is higher and the carrier mobility smaller and then will be less efficient to the THz generation process [70].

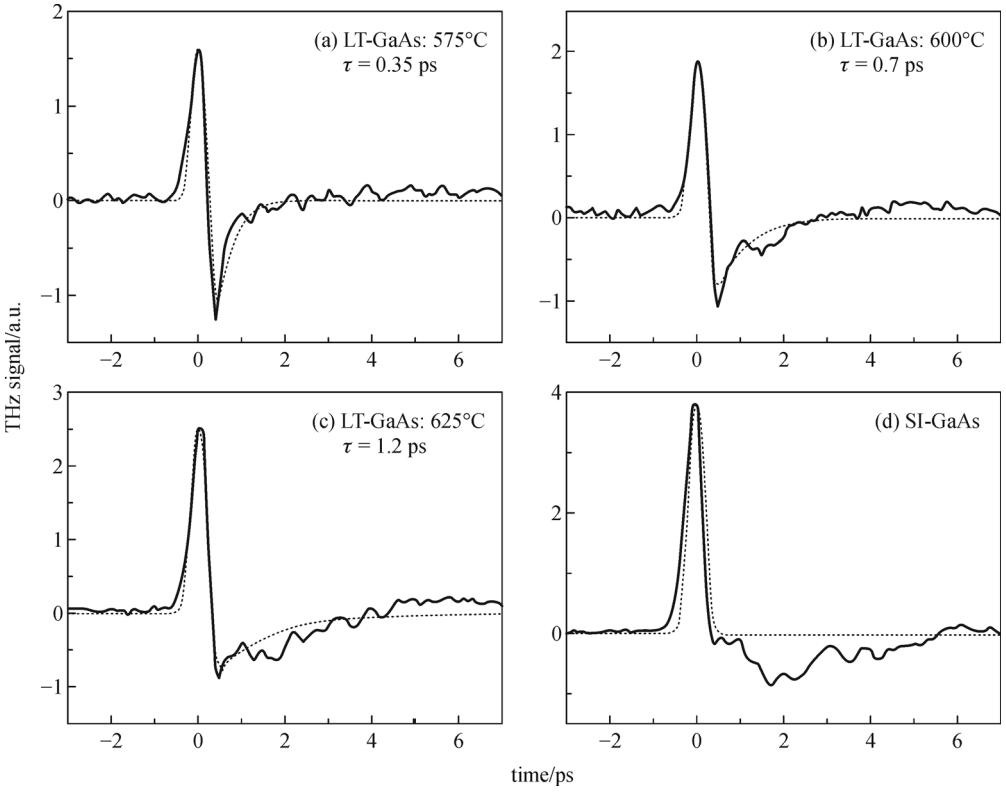

Fig. 4 THz radiation waveforms from LT-GaAs and SI-GaAs emitters with the excitation by low optical fluence single pulses. The solid lines represent the measured waveforms and the dashed lines represent the calculated waveforms. Emitter material: (a) LT-GaAs annealed at 575°C, (b) LT-GaAs annealed at 600°C, (c) LT-GaAs annealed at 625°C, and (d) SI-GaAs [67]

2.1.4 PCA failure

As previously mentioned, the most straightforward method to generate high-intensity THz pulses from LAPCA is to apply the highest bias field possible. The semiconductor substrate of a LAPCA, under the excitation of a femtosecond laser pulse, shows a rapid decay in its resistivity. Such low-resistivity substrate, when biased with high voltage, could lead to certain failures. It is well-known that photoconductive switches have a limited lifetime, from several shots up to millions of shots if the performances of the switch are pushed to the limit [79]. Among the most common failures observed in conventional PCAs is the thermal heating that leads to thermal runaway, corona discharge, surface flashover and dielectric breakdown. Dielectric breakdown happens when the electric field is strong enough to rip electrons from the valence band to the conduction band. Then this electron is accelerated by the electric field itself and gains kinetic energy. This electron can collide with another bound electron and get excited into the conduction band, creating another free electron. In the end, the rapid multiplication of free electrons leads to an avalanche dielectric breakdown where the semiconductor substrate becomes conducting [80]. The dielectric breakdown happens at lower fields for material with relatively low bandgap or when the quality of the substrate is poor with defects, high grain and high micro stripe density. It is intuitive to understand that dielectric breakdown by electron avalanche happens at a higher bias field when using low-bandgap semiconductors. On the other hand, flashover and corona discharge occurs when dust, grease or charge accumulation arises at one of the electrodes, and it suddenly discharges. These arcs gradually deteriorate both the substrate and electrodes, which considerably reduce the lifetime of the photoconductive emitter. However, in all cases of failure, the most common is likely the thermal runaway. The photocurrent that creates heat by the Joule effect and the power of the illuminated laser leads to the rise in the switch temperature. A study has shown that for a GaAs photoconductive switch, an increase of 25 degrees results in a drop in the bias electric field threshold by 40% [81]. In another work, some GaAs microstructure PCAs for THz generation have been investigated under X-ray diffraction topography [82]. It was shown that due to the increase in temperature, some electromigration of the gold electrodes occurred, resulting in a total electrical short-cut of the electronic circuit preventing the PCA to work (Fig. 5). Moreover, the GaAs substrate itself was degraded.

To prevent thermal runaway, it is preferable to choose semiconductor substrates with high thermal conductivity for dissipating the heat. In addition, it is important to realize high-quality Ohmic contacts on the substrate. Another option is also to have a substrate with a short carrier lifetime and high dark resistivity to limit the heating of the PCA by the current. Dark resistivity is the resistivity of the PCA when the switch is on the off-state and is mainly determined by the bandgap of the semiconductor substrate. The use of wide bandgap semiconductors with high dark resistivity reduces the heating of PCAs by lower dark current. Another option is to work with a semiconductor substrate with a short carrier lifetime. The short lifetime reduces the duration of the photocurrent, which is the specific moment where the heating by the Joule effect is stronger. Many techniques have been tested on GaAs semiconductor for decreasing the carrier lifetime. These studies are clearly described in the review on microstructure PCA for THz radiation from Burford and

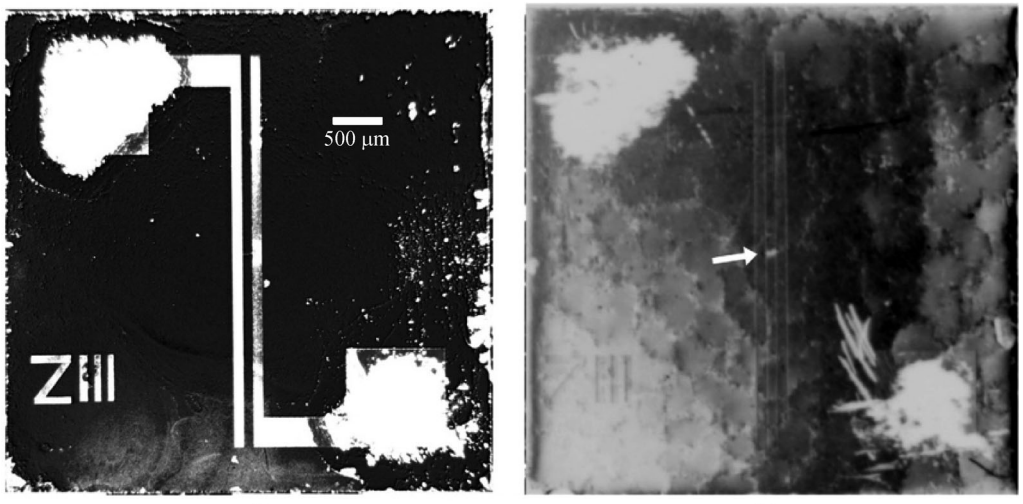

(a) (b)

Fig. 5 Optical micrograph of (a) failed antenna, (b) X-ray topography of the device showing considerably grain boundaries and domains as well as electro-migration of gold (arrow) in between the microstrips [82]

El-Shenawee [46]. Most of these GaAs PCA with short carrier lifetime show general performances that are better than SI-GaAs PCA and equivalent to LT-GaAs PCA. This was possible because the higher thermal stability of the PCAs allows applying a higher bias field, which in turn increases the maximum radiated peak electric field. To reduce the lifetime of carriers inside the GaAs substrates, one of these techniques is ion implantation. Recent studies have shown that ion implantation in GaAs semiconductors improves their carrier mobility compared to LT-GaAs, resulting in point defects within the crystal structure. These recombination centers in turn can significantly reduce the carrier lifetime [83,84]. GaAs doped with Ar^+ ions had the shortest carrier lifetime over semi-insulating and low-temperature grown GaAs substrates [85]. Using the same technique, several research groups have implanted ions such as oxygen, nitrogen and iron into GaAs crystals, resulting in very short carrier lifetimes [86,87].

2.2 Materials for the development of THz LAPCAs

In the previous section, we reviewed the different parameters of semiconductors substrates that would influence the intensity of the THz pulses radiated by LAPCAs. We mentioned that a high dielectric strength that is linked with a wide bandgap is the most critical parameter. Other important parameters are the carrier mobility for optimized efficiency and good thermal conductivity. From Table 1, one can see that diamond is probably the perfect material for generating intense THz radiation. A chemical vapor deposition (CVD) grown poly-crystalline diamond thin film was tested for the fabrication of a LAPCA with an interdigitated structure illuminated by an excimer laser [55]. In this study, by depositing an encapsulation layer, the applied bias field was increased up to 0.5 MV/cm. Although diamond LAPCA offers promising results, without saturation of the scaling of the THz field versus bias field, with an obtained radiated energy density as high as 10 μJ/cm^2, which is one order of magnitude larger than GaAs, with a bias field applied of 100 kV/cm, diamond PCA has not been intensively studied. This is due to its bandgap of 5.46 eV, which requires the 4th harmonic of an 800 nm Ti:sapphire laser or a two-photon absorption process with an excimer laser, which has limited until now its application. In addition, the cost of the diamond antenna dramatically reduces its attractiveness. For this purpose, ZnO and GaN are other wide-bandgap semiconductors that are used as promising materials for the fabrication of LAPCAs [57,61,88]. However, in the case of ZnO, the poor fabrication quality of the substrate, with many defects, leads to the saturation of the THz yield as a function of bias electric field for values as low as 0.8 kV/cm. In comparison, GaAs LAPCA has demonstrated linear scaling of the THz field versus bias field up to 50 kV/cm [89]. In the next section, we will examine the performances of ZnSe and SiC LAPCAs pumped above and below the bandgap by the 1st and the 2nd harmonic of a Ti:sapphire laser. Then, using an UV laser, we will review the performances of LAPCAs fabricated with different wide bandgap semiconductors and pumped by a UV laser with a photon energy of 5.0 eV.

2.2.1 Zinc selenide

Zinc selenide (ZnSe) has a bandgap of 2.67 eV and is widely used as optical windows and lens for the infrared region [9]. ZnSe substrates were also used as photo-conductive switches where switching of bias field above 100 kV/cm with a peak current of 100 kA/cm^2 with electrodes deposited on the two-opposite face of the substrate were achieved [91–93]. Due to these good performances, it was natural to test ZnSe PCA for THz generation. The ZnSe bandgap allows photo-excitation with Ti:sapphire laser via standard photon absorption (PA) when using the 2nd harmonic, and via two-photon absorption (TPA) when using the fundamental harmonic. In the first case, we will talk about above bandgap photoexcitation, and in the second case, about below bandgap photoexcitation. The first demonstration of THz radiation from ZnSe PCAs was done by Holzman and Elezzabi [94]. The PCA was an H-dipole geometry with a gap of 9 μm (Fig. 6(a)). By focusing an optical spot size, close to the anode at an excitation wavelength of 800 nm with below bandgap excitation, they demonstrate a linear scaling of THz field versus bias field up to 125 kV/cm and versus fluence up to 28 mJ/cm^2. The linear behavior of the scaling of the THz pulse versus bias field is very important since it is the major condition for scaling up the source for high-intensity THz pulses generation (Fig. 6(b)). Surprisingly, the peak electric field of the THz pulse scales linearly with the fluence up to 28 mJ/cm^2 without showing any sign of saturation. Indeed, the below bandgap photoexcitation leads to a TPA process, which is a nonlinear process and depends on the intensity of the laser pulse. However, there is no reason that the PCA would not show any saturation regime if the optical fluence keeps increasing. We note that these results are different from the observations in another work with THz wave generation via single-photon and TPA in ZnSe LAPCA pumped by an amplified Ti:sapphire laser [51]. This study shows the influence of the wavelength and the quality of the substrate on the THz generation from ZnSe LAPCAs [51]. For this study, ZnSe mono-crystalline and poly-crystalline substrates were used to fabricate LAPCAs with an interelectrode distance of 1 mm, with electrodes located on each side of the crystal to limit air-breakdown. The normalized waveforms of the THz pulses emitted from mono- and poly-crystalline ZnSe LAPCAs, as well as the corresponding power spectrum of radiated THz pulses obtained by Fourier transform, are shown in Fig. 7. The performances of mono- and poly-crystalline ZnSe

LAPCAs excited with 400 nm laser pulses were studied, and linear scaling of the THz peak field as a function of bias voltage and a hyperbolic behavior of the scaling of the peak field versus optical fluence were found. The major difference was in the value of the saturation fluence, which was measured to be 0.15 mJ/cm^2 for mono-crystalline ZnSe LAPCAs and 1.01 mJ/cm^2 for poly-crystalline ZnSe LAPCAs. The difference in the saturation fluence was attributed to the difference in carrier mobility between the two substrates.

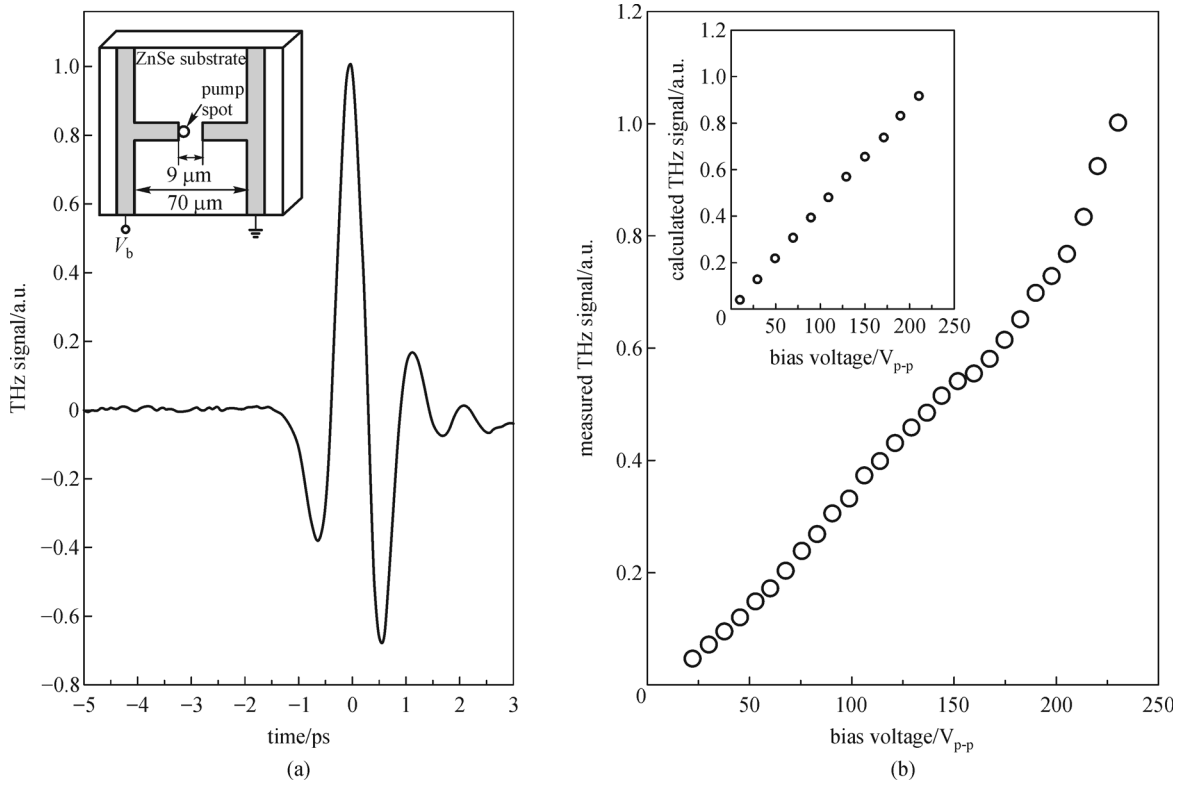

Fig. 6 (a) Time-domain waveform produced by photoexcitation of the ZnSe THz emitter with 160 mW pump beam and a 230 V_{p-p} bias voltage. The edge-illuminated PC gap and THz dipole emitter are shown in the inset. (b) Measured peak-to-peak THz field amplitudes as a function of the PC gap bias voltage. The THz waveform amplitudes calculated from the photocurrent transport model are shown in the inset [94]

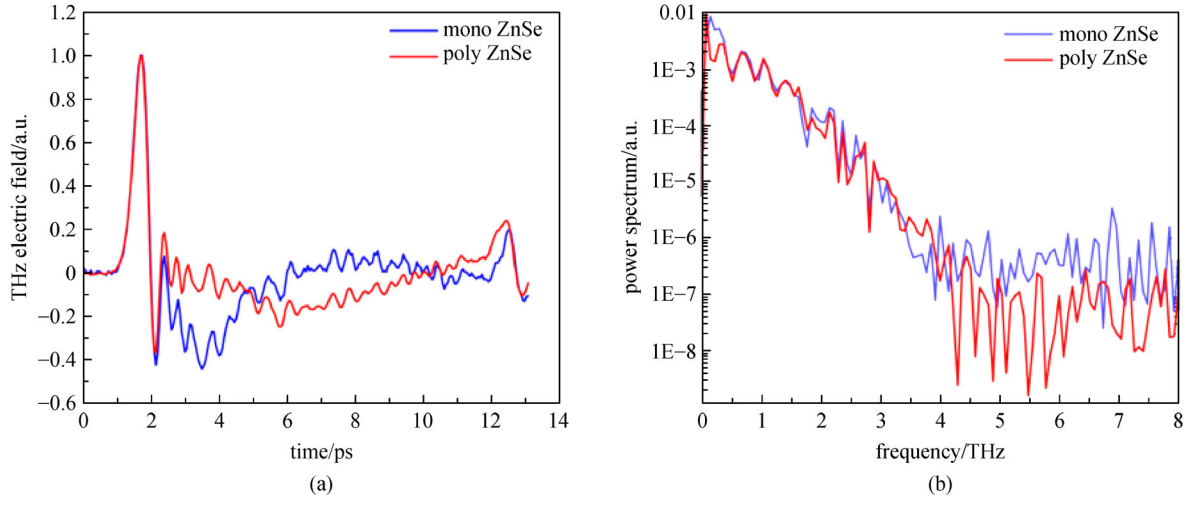

Fig. 7 (a) Normalized waveforms THz pulses emitted by mono- and poly-crystalline ZnSe LAPCAs. (b) Corresponding power spectrums to the THz pulses radiated that is obtained by Fourier spectrum [51]

Next, the authors studied the differences in the performance of mono-crystalline ZnSe LAPCA excited above and below the bandgap. As mentioned above, the scaling of the THz field follows a hyperbolic behavior versus optical fluence when pumped above the bandgap. On the other hand, when the ZnSe LAPCA is pumped below the bandgap, with 800 nm laser pulse, the scaling of the THz pulse follows a quadratic behavior for fluence below 0.7 mJ/cm^2, then it becomes linear for fluence up to 2.1 mJ/cm^2 and saturation starts to occur for fluence above 2.1 mJ/cm^2 (Fig. 8). More importantly, when the LAPCAs are working in the saturation regime, the field of the THz pulses generated by the mono-crystalline ZnSe LAPCAs saturates at the same peak field value for above and below bandgap. The only noticeable difference was that the ZnSe LAPCA pumped with 800 nm laser pulses was more fragile than when pumped with 400 nm laser pulses. This difference was attributed to the fact that the optical power and the Joule effect leading to the enhancement of the temperature of the switch, was stronger when the LAPCAs were pumped below the bandgap than above the bandgap.

Next, they compare the performances of mono- and poly-crystalline ZnSe LAPCAs pumped above the bandgap with GaAs LAPCAs pumped above the bandgap with an 800 nm laser and with the same electrode configuration (Fig. 9). The scaling of the THz field versus optical fluences was hyperbolic for the three antennas. Of course, due to the difference in carrier mobility between the three substrates, the saturation fluence of the three LAPCAs were quite different (0.01, 0.15 and 1.07 mJ/cm^2 for GaAs, mono- and poly-crystalline ZnSe LAPCAs, respectively). However, it is quite fascinating that the value of the THz peak field once the LAPCAs operate in the screening regime was the same for the three antennas.

The last part of the study was to compare the scaling of the THz peak field as a function of the bias field for the mono-crystalline ZnSe LAPCAs and the GaAs LAPCAs

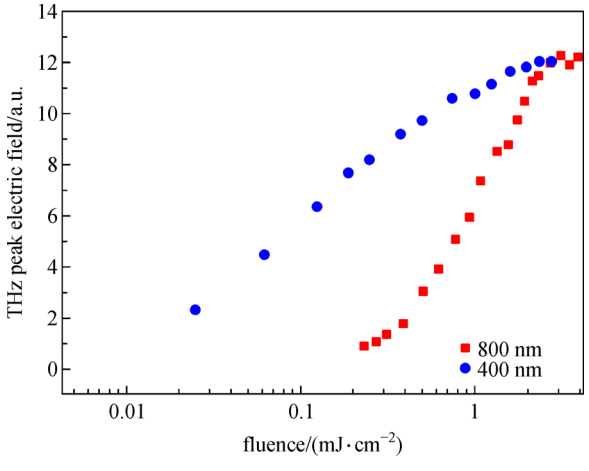

Fig. 8 Fluence dependence of the peak THz electric field from ZnSe single crystal antenna illuminated at 400 and 800 nm [51]

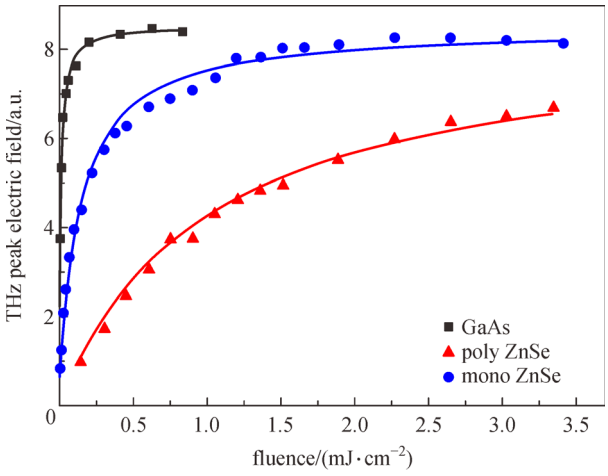

Fig. 9 Fluence dependence of peak field of THz radiation from GaAs, ZnSe single crystal, and poly-crystalline ZnSe PCA. Squares are the experimental data, and solid lines are fits to the data [51]

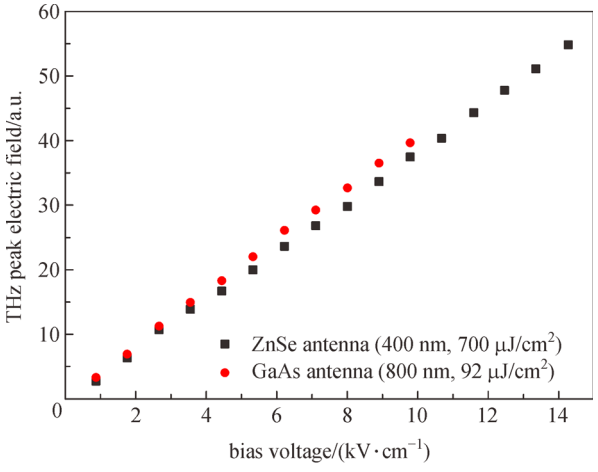

Fig. 10 Comparison of bias field dependence of the peak THz electric field for GaAs antenna excited at 800 nm and mono-crystalline ZnSe antenna excited at 400 nm [51]

(Fig. 10). The two curves show linear behavior with approximately the same slope. However, while the GaAs LAPCAs breakdown at a bias field around 10 kV/cm, the ZnSe LAPCA took advantage of its higher dielectric strength and was able to sustain higher bias voltage. Consequently, the peak electric field of THz pulses generated by the ZnSe LAPCAs was larger than the one generated by the GaAs LAPCA.

2.2.2 Silicon carbide

Silicon carbide (SiC) has dielectric strength and thermal conductivity that are more than ten times higher than GaAs crystal with relatively good carrier mobility. These semiconductors are also extremely resistant to damage,

such as corona discharge due to their extreme hardness. In addition, good electrical properties and excellent thermal stability make these semiconductors an ideal candidate for manufacturing high-power electronic devices such as Schottky barrier diodes, MOSFETs and photoconductive switches [95,96]. For 4H-SiC photoconductive switches with lateral configuration, pumped with 7 ns laser pulse duration at 355 nm, the switching of 20 kV DC voltage for an equivalent bias electric field of 328 kV/cm was demonstrated. The fact that the substrate holds this bias field was possible due to the significant improvement made on the growth of high-quality SiC substrate and especially 4H-SiC [97,98]. Some damages were also observed, and applying such a field creates some holes at the interface between the contact and the substrate [99]. We note that applying such a bias field onto a SiC LAPCA would generate gigantic low-frequency half-cycle THz pulses, which would open the door for new physics such as fast magnetization switching by a single pulse [100]. As a consequence, LAPCAs based on SiC polytypes having hexagonal symmetry with double (4H) and triple (6H) stacking periodicities pumped by ultrafast laser pulse for THz radiation were naturally tested. The LAPCAs made from semi-insulating 6H-SiC semiconductors were pumped using 800 and 400 nm laser pulses. 4H-SiC LAPCAs were pumped only using a 400 nm laser beam. Figure 11(a) shows the normalized waveform, and in the inset is the original waveforms, and Fig. 11(b) shows their normalized amplitude spectra of the THz pulses radiated by the 6H- and the 4H-SiC LAPCAs [63].

The authors demonstrated a linear scaling of the THz field versus the bias field in all conditions for a bias field up to 32 kV/cm. In this case, linear behavior was demonstrated (Fig. 12). Also, the scaling of the electric field of THz pulses generated by the 6H-SiC LAPCAs only showed a standard hyperbolic behavior in the scaling of the radiated THz field versus optical excitation when pumped with 400 nm laser pulse (Fig. 13). The saturation fluence was found to be around 0.24 mJ/cm^2, which is close to the saturation fluence obtained with ZnSe LAPCAs. Despite the higher carrier mobility of 6H-SiC, this saturation fluence recorded for LAPCAs is higher than the estimated value. This difference in value was explained by the fact that the 6H-SiC is an indirect bandgap semiconductor, which is partially transparent at the 400 nm wavelength. Consequently, each electron that is injected into the conduction band requires a photon and a phonon. This decreases the quantum efficiency of the free carrier generation process.

Under an optical excitation at 800 nm, the 6H-SiC LAPCA shows a similar scaling behavior in the THz field to that of the ZnSe LAPCA when pumped with a laser beam at 800 nm. This was expected since, in this case, the absorption process for the two substrates is two-photon absorption. Despite pumping the LAPCA up to 9 mJ/cm^2, the LAPCA was still not running in the screening regime. More surprisingly, the scaling of the electric field of THz pulses radiated by the 4H-SiC LAPCA pumped by a 400 nm laser pulse was a mixture between a quadratic behavior for optical fluence lower than 1 mJ/cm^2 and a hyperbolic behavior for higher fluences. This was explained by the fact that at low optical fluence, the TPA process was dominating since the bandgap of 4H-SiC is 3.26 eV, which is slightly higher than the photon energy at

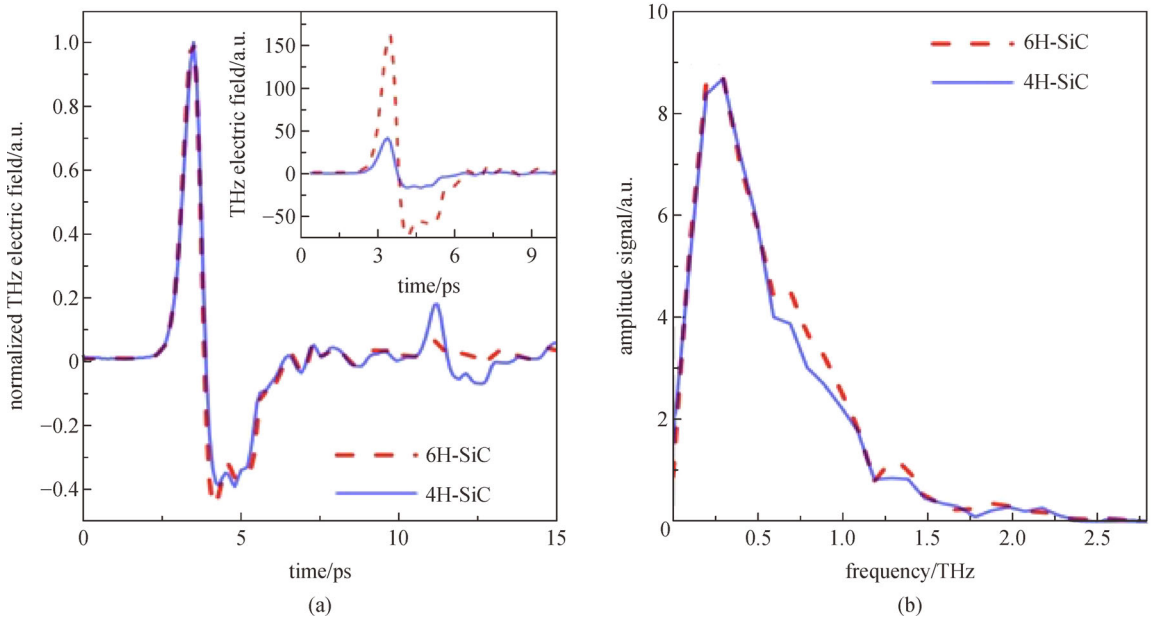

Fig. 11 (a) Normalized and in inset original THz waveforms radiated by 6H- and 4H-SiC LAPCA antennas excited at 400 nm with a fluence of 0.29 mJ/cm^2 and biased at 9.25 kV/cm. (b) Their respective normalized amplitude spectra [63]

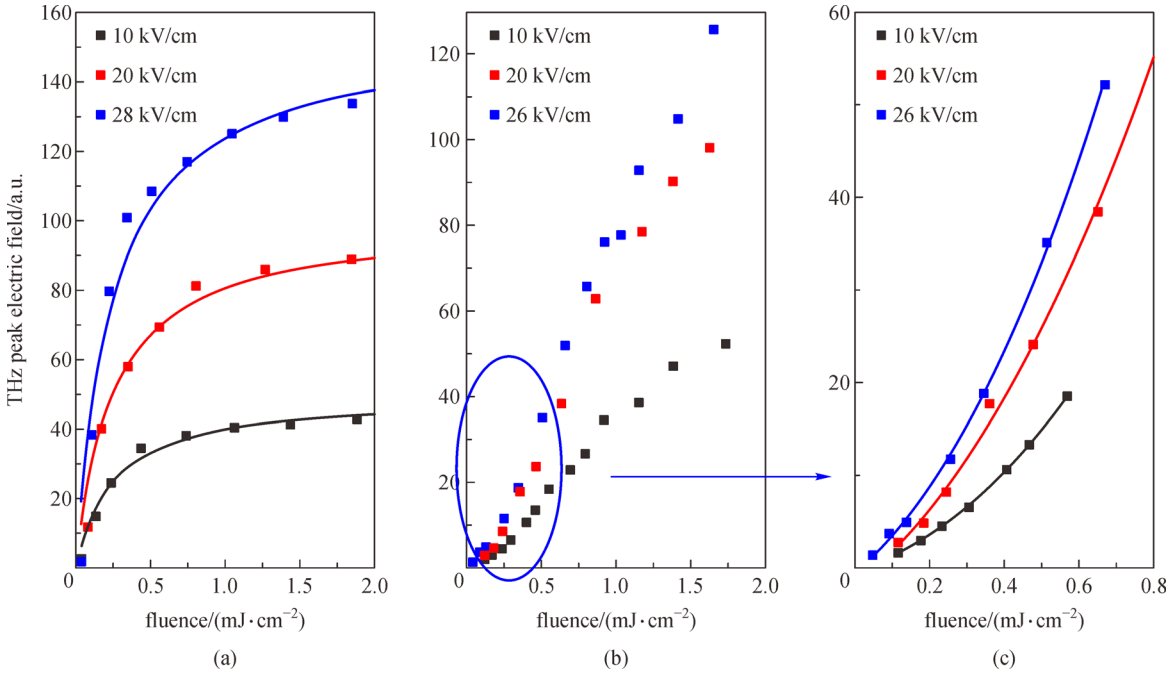

Fig. 12 THz peak electric field versus fluence for a 6H-SiC (a) and 4H-SiC (b) PC antenna excited at 400 nm and biased with three different bias fields. (c) is an expanded scale of the bottom left part of (b), in order to show the quadratic dependence of the field on fluence for the 4H-SiC PC antenna at low excitation fluence [63]

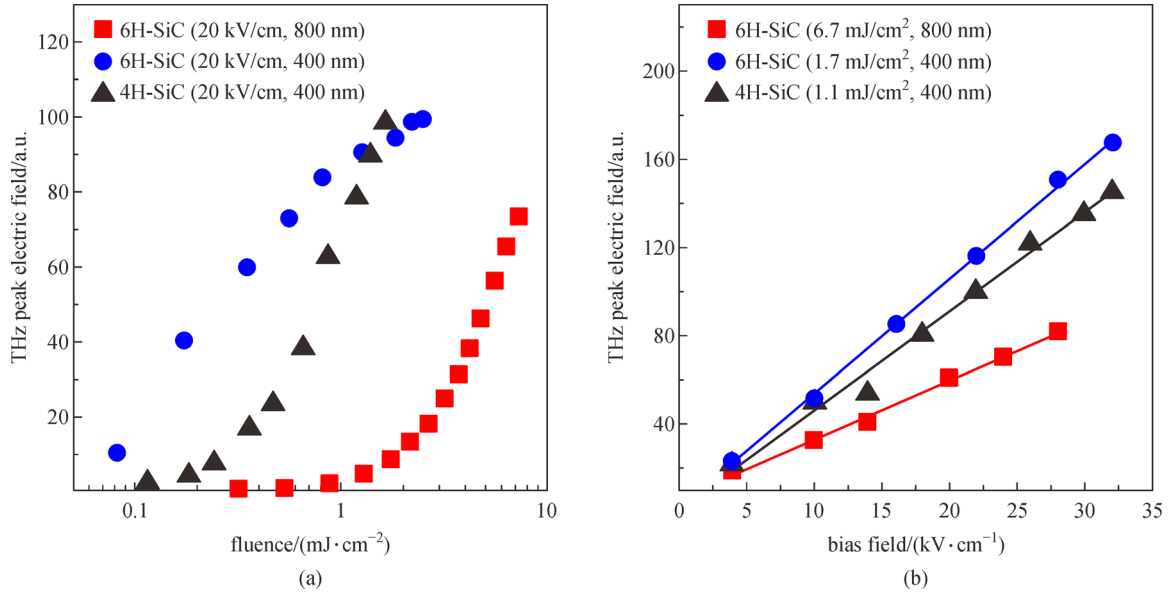

Fig. 13 (a) THz peak electric field versus fluence for 6H-SiC PCA excited at 400 and 800 nm, and for 4H-SiC PCA excited at 400 nm and biased at 20 kV/cm. (b) THz peak electric field versus bias field for 6H-SiC PCA excited at 400 nm at 1.7 mJ/cm^2 and 800 nm at 6.7 mJ/cm^2, and for 4H-SiC PCA excited at 400 nm at 1.1 mJ/cm^2 [63]

400 nm wavelength (3.10 eV). However, by increasing the optical fluence, the onset of saturation appears, which is due to the screening of the bias field by the THz field. The screening regime appears at much higher fluence for the 4H-SiC LAPCAs in comparison with the 6H-SiC LAPCAs, although the carrier mobility is higher.

2.2.3 Large bandgap semiconductors excited by UV lasers

As we have previously discussed, to take maximum advantage of LAPCAs made with wide-bandgap semiconductors pumped by the 2nd harmonic of a Ti:sapphire laser, the bandgap of the semiconductor substrate is limited

to 3.1 eV for maximizing the photon absorption. To extend the choices of the semiconductor crystal, one solution is to work with lasers that have their fundamental wavelength shorter than 400 nm. Excimer lasers are a family of high pressure, pulsed gas lasers that produce intense UV light [101]. The wavelength of these lasers is determined by the gas gain media of the laser ranging from 193 to 353 nm [102]. Also, with specific configurations, the duration of the laser pulse can be compressed to a few hundreds of femtosecond and even shorter [103–105]. As we mentioned earlier, the diamond PCAs have been studied using a KrF laser with a pulse duration of 500 fs at 248 nm [55]. The photoconductive emitters based on GaN semiconductors have also been studied under the excitation of the 3rd harmonic of a Ti:sapphire laser with a pulse duration of 120 fs and the energy of 19 J/pulse, respectively at 266 nm [61]. In addition, GaN PCAs have been recently studied using driving laser pulses at 352 nm from an optical parametric amplifier (OPA) [106]. All these studies show high potential for the generation of intense THz pulse from LAPCA with wide bandgap semiconductor crystal pumped by a UV laser. However, there was no direct comparison of their performances as a substrate of LAPCAs.

Recently, a study was performed on the THz radiation from LAPCAs fabricated from ZnSe, 6H- and 4H-SiC, GaN and β-Ga_2O_3 using KrF laser excitation at 248 nm, which allowed a direct comparison of their performances [35]. The main reasons why these crystals have been selected are because most of them have been tested previously for THz generation from PCA. In addition, these semiconductors have a bandgap of less than 5 eV with high dielectric strength and commercially available with relatively large wafer sizes. The design of all the LAPCAs studied was the same, with the electrode length and gap size of 15 and 3 mm, respectively, using Cr/Al electrode deposition. To excite these photoconductive emitters, a hybrid dye-excimer laser (KrF) with pulse energy and duration of 30 mJ and 500 fs, respectively, at

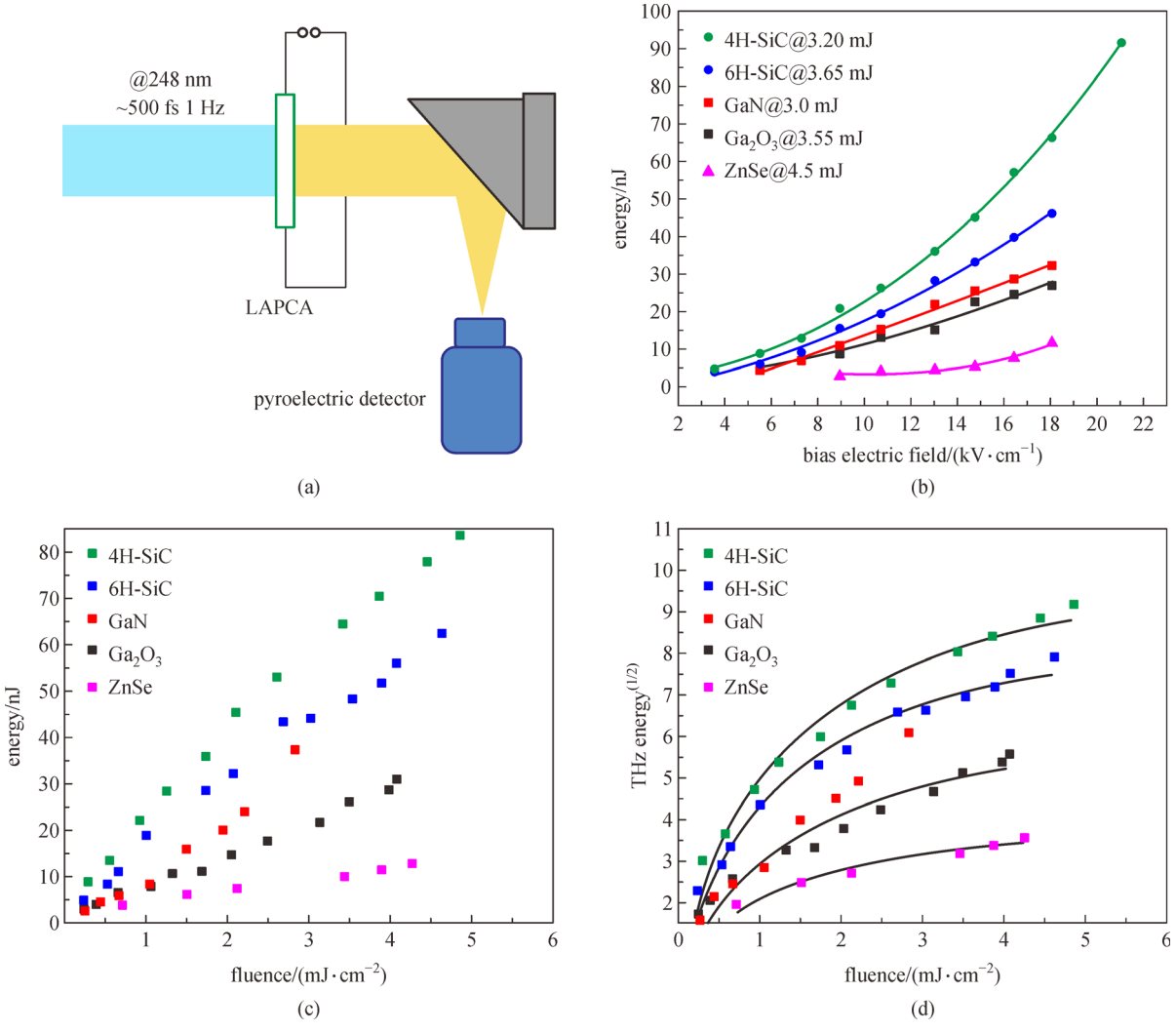

Fig. 14 (a) Experimental configuration. (b) Scaling of the THz energy as a function of the bias field. (c) Optical fluence for 4H-SiC, 6H-SiC, GaN, β-Ga_2O_3 and ZnSe LAPCAs. (d) Scaling of the square root of THz energy as a function optical fluence [35]

248 nm is used [107]. The scaling of the energy of the THz pulses as a function of bias field and optical fluence is shown in Fig. 14. The authors showed that the 4H-SiC and the 6H-SiC emitted the maximum THz pulse energy in this configuration, which was followed by GaN, β-Ga_2O_3 and ZnSe LAPCAs, in descending order. As can be seen from Fig. 14, at a bias field of 18 kV/cm and an optical fluence of 3 mJ/cm^2, the energy of THz pulses radiated by the 4H-SiC LAPCA was 1.5 and 2 times higher than that of the 6H-SiC and the GaN LAPCAs, respectively. For almost all antennas, the scaling of the THz energy was quadratic with the bias field and mostly hyperbolic with the optical fluence. When the optical fluence was high enough, the scaling of the THz energy reached a saturation regime. The latter observation is in good agreement with theory. Surprisingly, despite the significant differences in their carrier mobility, all the LAPCAs studied have shown almost the same saturation fluence of around 1.2 mJ/cm^2. Indeed, the calculated carrier mobility is between 50 and 60 cm^2/(V·s), which is approximately one order of magnitude smaller than the theoretical values. This difference is attributed to the fact that the 5.0 eV photon energy of the 248 nm laser pulse pumps the electrons into the higher valley of the conduction band, where the effective mass of the electron is higher with smaller carrier mobility. We note that the carrier mobility of 4H- and 6H-SiC, β-Ga_2O_3 and ZnSe are close to that of GaN LAPCA when pumped by a 266 nm laser pulse and 120 fs duration [35]. Also, the observed difference in performances of the LAPCAs studied can be explained by the difference of inter- and intra-valley carrier dynamics of the semiconductor substrates [70–72]. However, to fully understand the scattering mechanisms, additional measurements such as optical pump/THz-probe spectroscopy is needed [108].

In this section, we reviewed the principal results on LAPCAs, demonstrating their potential for generating intense THz pulses. We have shown how wide-bandgap semiconductor crystals are well adapted for the generation of intense THz pulses when excited by the second harmonic of a Ti:sapphire or UV laser pulses. Our research has shown that, except for two works with GaAs LAPCAs pumped by 800 nm laser pulses, there does not exist any demonstration of the generation of intense THz pulses with LAPCAs with peak field above 100 kV/cm [39,109]. The major reason is that these THz devices require a large area with very high pulse voltage up to several tens of kV [110]. Such pulsed, high-voltage sources are dangerous to handle and expensive. To overcome this challenge, one solution is to work with ILAPCA, which keeps the size of the antenna large while reducing the gap size, thus avoiding the use of very high voltage pulses. One parameter that we did not mention is the electrodes configuration. Many works have shown that the configuration of electrodes onto the PCAs is an important parameter that influences the efficiency and the maximum intensity of the radiated THz pulses [46,47]. It was shown that the largest power was obtained with a SI-GaAs bowtie PCA. However, these sources are not well adapted to generate THz pulses with high peak intensity, like plasmonic antennas, since their configuration is not scalable to a larger area, so we did not develop this part. Another characteristic of PCA, with a specific electrode configuration, you can manipulate the polarization of the radiated THz field. For example, THz pulses with longitudinal, radial and azimuthal polarization have been demonstrated [111,112].

3 Interdigitated large-aperture photoconductive antennas

The idea of working with ILAPCAs was taken from the interdigitated photoconductive switch technology, which was studied in the mid-1980s [113,114]. ILAPCA simply consists of a pair of anode and cathode, which are connected to several open-ended parallel electrode-combs (Fig. 15). As a consequence, ILAPCA is an array of small photoconductive antennas that are connected in parallel. Consequently, two adjacent open-ended electrodes with the same gap size will generate THz pulses having opposite polarity, which will interfere destructively when propagating in the far-field [73,115–119]. Therefore, it is necessary to block the illumination of all antennas biased with one specific bias field direction (positive or negative) by using, for example, a shadow mask. Thus, destructive interferences are avoided by generating carriers only in gaps with the same polarity of the applied bias field. Consequently, by blocking the incident optical excitation in every second inter-electrode spacing, and therefore performing photogeneration only in regions with the same bias field directions, constructive interference of pulses emitted with the same polarity will improve the overall far-field THz emission performance [120]. Traditionally this process is performed during the fabrication process of the ILAPCA by the photolithography technique. After the deposition of electrodes onto the substrate, a thin dielectric layer, such as SiO_2, is deposited on the top of the electrodes, followed by the deposition of a metal layer only onto the neighboring antenna. The role of the second metallic layer is to reflect the incoming laser pulse avoiding the illumination of the neighboring antenna, while the role of the dielectric layer is to avoid electronic short-circuit between the electrodes and the second metallic layer. The inter-electrode spacing of the antenna is traditionally limited by the thickness of the deposited dielectric layers. Since the thickness of deposited dielectric layers is limited, the maximum gap-size of the antenna is restricted. ILAPCAs offer several advantages over conventional LAPCAs. As we mentioned earlier, the reduced distance between cathode and anode allows large bias fields to be applied without the need for a very high voltage power supply. The drop in applied bias voltage reduces the

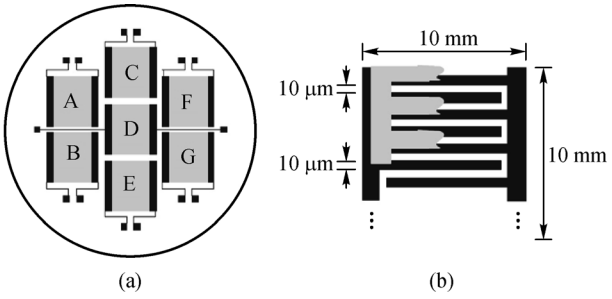

Fig. 15 (a) Schematic of THz emitter composed of seven photoconductive antenna units having interdigitated electrode structure. The units are labeled A–G for later reference. (b) Structure of electrodes and shadow mask of each unit [115]

heating of the ILAPCAs by the Joule effect and prevents antenna failure allowing a higher bias field to be applied. Also, the maximum bias field applied is limited by the air breakdown on the antenna surface [121]. It has to be noted that this encapsulation layer for the improvement of the maximum bias applied field can also serve as an anti-reflection coating, improving the photon absorption [63,122,123]. Further, the trap field enhancement, which is just an enhancement of the bias field localized close to the anode, is multiplied due to the multiplication of the number of anodes inside the comb [49,70,124].

Besides these advantages, ILAPCAs have some drawbacks. The biggest one is that by using a standard shadow mask on the interdigitated structure, only half of the total antennas will be illuminated. If we add the surface of the electrodes, where in some cases the electrode width is equal to the inter-electrode distance, only 25% of the total surface of the ILAPCA will be illuminated and will efficiently participate in the generation of THz radiation [89]. This reduces the maximum radiated peak electric field and efficiency of the ILAPCA. Another drawback is that by adding the second metallic layer on the top of the interdigitated structure, the inter-electrode distance is more or less limited by the maximum thickness of the dielectric layer, which is generally limited to a few tens of μm before cracks start to appear. Consequently, the gap size is chosen to be in the tens of μm range or smaller [125], which limits the maximum radiated THz field due to the appearance of strong space-charge screening at a timescale shorter than 1 ps. The other consequence is that the waveforms of the THz pulses change from quasi-half cycle to a single cycle. Finally, the multiplication of the number of antennas inside the interdigitated structure increases the capacitance significantly, which can, in turn, distort the high-voltage pulse for biasing the ILAPCA but also reduce the maximum radiated power [126–128]. Another point is that ILAPCA has a large area with a diameter much larger than the wavelength of the radiated THz waves. Therefore, we expect a THz beam divergence that is relatively small. However, the inter-electrode distance is smaller or equivalent to the radiated wavelength, while the electrode length will be much larger than the radiated wavelength. Consequently, the beam divergence will be quite different for the direction perpendicular versus the direction paralleled to the electrode orientation. As a result, it is generally challenging to focus the THz beam close to the diffraction limit, which is one of the key points for achieving a large peak field.

3.1 Overview of ILAPCAs

To overcome the limitations of conventional LAPCAs with the goal of increasing the peak intensity of emitted THz pulses, several works have focused on ILAPCAs [35,55,89,115,116,129–131]. One of the key points was the demonstration of increased intensity of the THz pulses emitted by ILAPCAs compared to THz pulses generated by conventional LAPCAs. The first comparison was made by Hattori et al. [115] where they compared the intensity of THz pulses generated by a conventional SI-GaAs LAPCA with 3 cm gap size with an ILAPCA with 7 units with an area of 1 cm^2 each, connected together, with gap size and electrode width equal to 10 μm for a total illumination area of 25%. Although the ILAPCA was biased at 30 kV/cm, compared to only 2 kV/cm for the LAPCA, the THz pulses generated from the LAPCA was 2 times larger than the one from the ILAPCA (Fig. 16(a)). Following the scaling law of the peak amplitude of the THz pulses as a function of the illuminated area, the peak field of the THz pulses emitted by the ILAPCAs should have been 7 times larger than the peak electric field of the THz pulses emitted by the conventional LAPCAs. The authors explained that the difference in amplitude of the emitted THz pulses was due to insufficient charge supply within the ILAPCA due to the small gap size. However, we believe that a 10 μm gap size of SI-GaAs ILAPCA can lead to a strong static Coulomb field that screens the bias field, which is the origin of the space charge screening, which could explain this difference [42]. This hypothesis is supported by the observation that the waveforms of THz pulses generated by the LAPCA and the ILAPCA are completely different. The waveforms of the THz pulses generated by the LAPCA are asymmetric and quasi-half cycle, while the waveform of the THz pulse generated by the ILAPCA is a single cycle and symmetric, which is a sign of space-charge screening. Another theoretical study shows that the amplitude of the generated THz pulses from a GaAs ILAPCA is 3 times larger than the peak electric field radiated by a dipole antenna. However, although the optical fluence and applied bias field remain constant, the illuminated area of the PCA with an interdigitated structure was larger than the one of the dipole antenna, which makes it difficult to directly compare the performance of both antennas [124]. Using the same approach, Dreyhaupt et al. showed that the amplitude of the THz pulses emitted by a SI-GaAs ILAPCAs is 20 times larger than those of a SI-GaAs

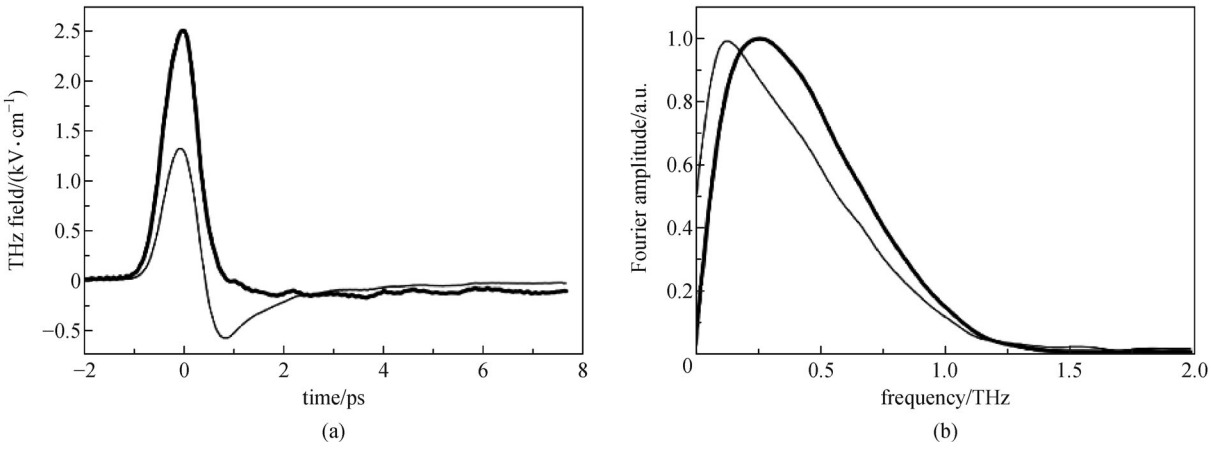

Fig. 16 (a) THz waveforms obtained from a conventional LAPCA (thick line), and micro-structured antenna array (thin line) under typical operation conditions. (b) Normalized spectrum of THz fields obtained from conventional large-aperture emitter (thick line), and micro-structured antenna array (thin line) [115]

dipole antenna [132,133]. However, due to the difference in the size of the illuminated area, it is difficult to make a direct comparison of the performance of both antennas.

One of the key aspects in ILAPCAs is to manipulate the antenna structure to control the specific parameters of the THz pulses emitted or to increase the efficiency and performance of the antenna. For example, there are different techniques for blocking the illumination of the neighboring antenna. One of them consists of using a large-aperture microlens area with a hexagonal structure to lead the beam direction onto every other antenna of the interdigitated structure [134,135]. The latter enhances the efficiency of the ILAPCA since all the optical energy is used to illuminate its active area. Another technique consists of suppressing one bias field direction by etching the active area of the neighboring antennas [136]. This technique is demanding in terms of cleanroom microfabrication because a thin semiconductor layer needs to be transferred onto an insulating substrate and etched into grooves. The last step consists of the deposition of metal electrodes on this structure. With this technique, using an LT-GaAs ILAPCA, the generation of THz pulses with peak field up to 120 kV/cm was demonstrated [131].

Another technique that could replace the deposition of the second metallization is the binary mask. The latter allows the entire illumination of the interdigitated structure by delaying the timing of the antenna illumination with the opposite bias field direction. This avoids the destructive interference from the quasi-half cycle THz pulses with opposite polarity since a time delay is introduced between them [38]. Indeed, the binary mask is only composed of a piece of glass that is transparent at the wavelength of the optical pump. As a result, we achieve first the generation of quasi-half cycle THz pulse for each antenna that is not covered by the mask, followed, after a time delay, by the generation of another quasi-half cycle pulse with opposite polarity, coming from the neighboring antenna covered by the mask. By adjusting the time delay, which is proportional to the mask thickness, and by mixing the glass piece with some opaque pieces, it is possible to perfectly control the waveform of the THz pulses and to perform THz pulse shaping. Consequently, increasing the thickness of the phase mask increases the time delay between the positive and negative polarity of the THz pulses. Further, the optical-to-THz conversion efficiency, as well as the energy of the THz pulses emitted by ILAPCAs can be doubled (Fig. 17). Another parameter that influences the intensity of the THz pulses generated from the ILAPCA is the interdigitated structure itself. It has been demonstrated that increasing the width of the anode, for substrates having much higher electron mobility than hole mobility can greatly increase the amplitude of the THz field [137]. The enhancement in the THz pulse amplitude was attributed to the plasmonic oscillation induced by electrons arriving at the anode. Singh et al. demonstrated that changing the anode width from 2 to 50 μm could increase the peak field of the emitted THz pulses by up to 7 times [137]. However, for an electrode width over 50 μm or for an antenna with a gap size larger than the radiated wavelength, this effect tends to saturate [138].

In terms of efficiency, selecting an electrode width equal to the inter-electrode distance when using a shadow mask is the worst configuration since only 25% of the total area of ILAPCA is effective for illumination when using a shadow mask. One solution for increasing the active area of the ILAPCA is to have a gap size larger than the electrode width [126]. However, this ratio of the effective area illuminated can be further increased by reducing the dark gap size relative to the bright gap size and optimizing the width of the anode. It has been demonstrated that an ILAPCA with a gap size, anode and cathode width, and dark gap size of 20, 10, 5 and 5 μm, respectively, results in

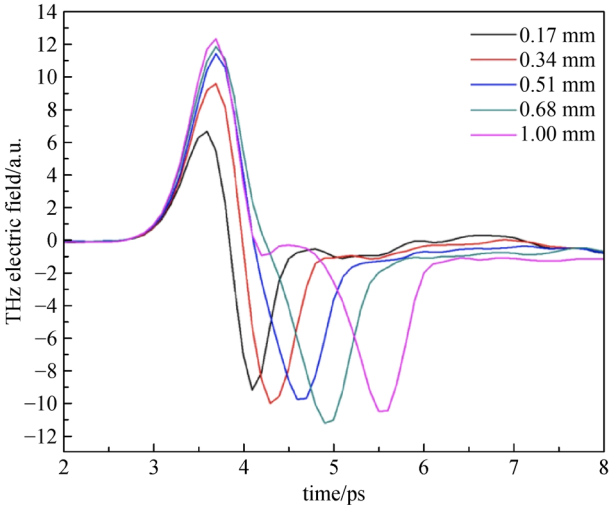

Fig. 17 Evolution of the THz pulse shape for different glass phase mask thickness (0.17, 0.34, 0.51, 0.68, and 1.00 mm thick) of an interdigitated GaAs LAPCA at a bias field of 1.2 kV/cm and a excitation fluence of 14 μJ/cm^2 [38]

an enhancement of 1.5 times in the radiated THz peak field compared with an ILAPCA with the same area but reduced gap size and anode width of 5 μm each [139]. This relative improvement is attributed to the plasmonic effect occurring near the anode and to the acceleration of the carrier within the substrate where the illuminated surface has been doubled from 25% to 50%. While playing with the parameters of the interdigitated structure, we can achieve a significant improvement in the THz intensity, it is also possible, by reducing the distance of the bright gap, to modify and compress the waveform of the THz pulses, which leads to a broadening of the THz spectra [140]. By using a 2 μm gap size for a semi-insulating GaAs ILAPCA, the generation in reflection mode of THz pulses with frequencies extending up to 20 THz has been demonstrated. The enhancement of the cut-off frequency was to the detriment of the peak electric field, which was reduced due to the strong space-charge screening effect [141].

Pushing the microfabrication technology to the extreme, the interdigitated PCAs were manufactured with an electrode comb having nanometric gape size [142]. These plasmonic photoconductive emitters have shown significant enhancement in THz power and optical-to-THz conversion efficiency up to 50 times over standard micro-PCAs, with a conversion efficiency of 1.6% for an interdigitated structure (Fig. 18). Despite their impressive performance, these antennas are not considered as large-area emitters due to their limited dimensions (less than a few mm), which is the key aspect for the generation of intense THz pulses [123]. Another key aspect parameter of the interdigitated structure is its ability to fully control the amplitude and degree of polarization of the THz field emitted. Indeed, by building an ILAPCA with an intermixed sickle geometry, with vertical and horizontal electrodes allows generating THz waves with horizontal and vertical polarization (Fig. 19) [143]. It has been shown that the generation of THz pulses with amplitude and degree of polarization can be controlled by applying different voltages to the vertical and horizontal electrodes. The speed of this photoconductive device for polarization modulation can reach up to 10 kHz, which opens new perspectives for THz polarimetry with detection locking for measurements of small polarization changes.

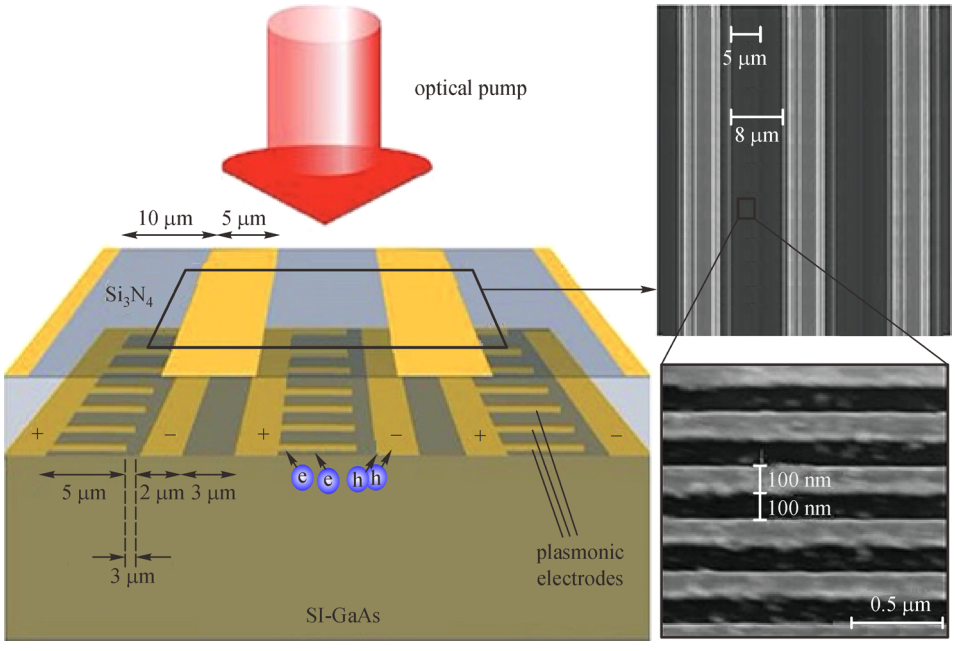

Fig. 18 Schematic and scanning electron microscope images of a large area plasmonic photoconductive source fabricated on a SI-GaAs substrate [29]

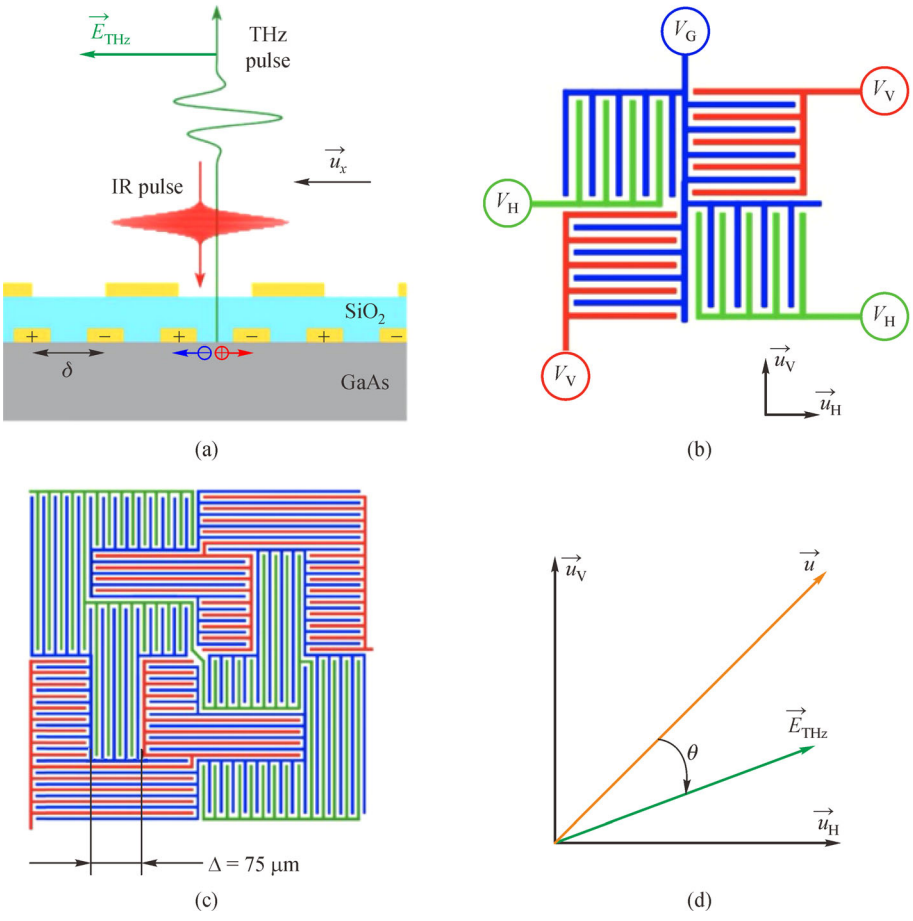

Fig. 19 (a) Cut view of an interdigitated photoconductive switch. Interdigitated gold electrodes on top of the GaAs layer consist of 4 μm wide electrodes, equally spaced by a distance Δ = 4 μm. (b) Top view of the intermixed geometry principle (only the first metallic layer is represented). (c) Large area implementation investigated experimentally with total area of the gold finger electrodes is 450 μm × 450 μm. (d) Orientation of the wire-grid polarizer $\vec{u}$ with respect to the interdigitated structure directions $\vec{u}_H$, $\vec{u}_V$ for the emitted field experimental characterization [143]

3.2 Generation of intense THz pulses from ZnSe and 6H-SiC ILAPCAs excited by femtosecond laser pulses

As we described in Section 2, the best and easiest way to generate intense THz pulse from LAPCAs is to work with wide bandgap semiconductor crystals. We described that ZnSe and 6H-SiC LAPCAs showed promising results when excited by the second harmonic of an amplified Ti:sapphire laser. Consequently, the next step was to fabricate a ZnSe and 6H-SiC LAPCAs with an interdigitated structure [38]. To this end, the first ILAPCAs were manufactured using a poly-crystalline ZnSe substrate. The antenna electrodes have been deposited using a standard photolithography technique. The ILAPCA structure was composed of 24 open-ended microstrip electrodes with a bright gap size equal to the dark gap size with a dimension of 0.6 mm, and electrode length and width of 22 and 0.4 mm, respectively. The gap size of the antenna was large enough to allow the ILAPCA to work in the screening regime rather than in the space-charge screening regime. The ILAPCA proposed was covered with a shadow mask or a quartz binary mask with a thickness of 0.65 and 1 mm. The active illuminating area was 1.5 and 3.0 cm^2 when using the shadow and the binary mask, respectively. The waveforms of the THz pulses generated by ILAPCAs covered by the three masks or a combination of shadow and binary mask are shown in Fig. 20. One can clearly observe that the THz pulses are changing from a quasi-half cycle to a single-cycle waveform with significant degrees of freedom between the two, offering full control of the generated waveform. More importantly, when excited with a 10 Hz, 400 nm and up to 20 mJ of optical energy, the energy of the THz pulse generated from the ILAPCAs covered with the 1 mm mask is 1.7 larger than that generated by the shadow mask when the ILAPCA is biased and excited with the same parameters. The maximum energy of the THz pulses was found to be 3.6 μJ when the ILAPCA was biased at 47 kV/cm, excited with a

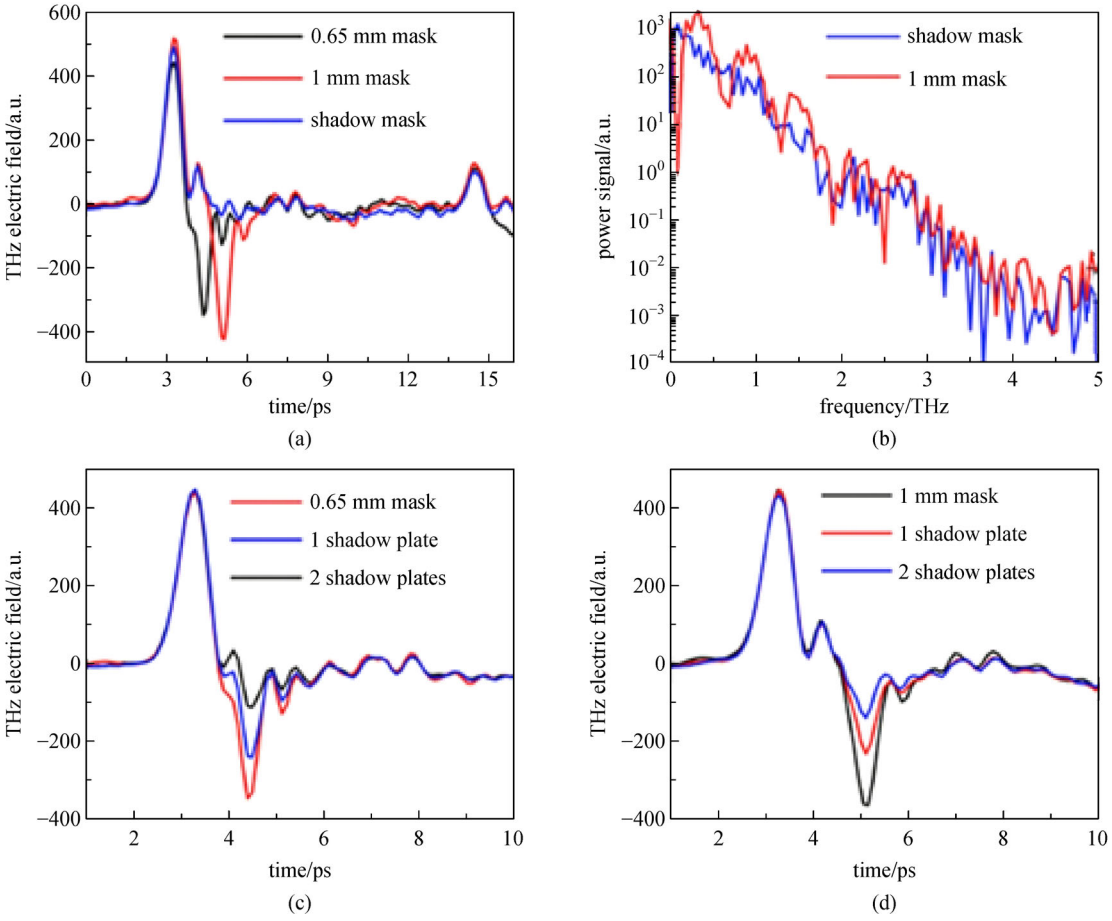

Fig. 20 THz pulses shapes generated from the ZnSe interdigitated LAPCA excited at 400 nm with a fluence of 0.2 mJ/cm^2, at a bias field of 10 kV/cm with 0.65 and 1 mm binary mask and a shadow mask. (b) Power spectrum with a shadow mask (blue line), and the 1 mm binary mask (red line). (c) and (d) THz pulse shapes obtained with the 0.65 mm (c) and the 1 mm (d) binary mask on the ZnSe LAPCA [38]

fluence of 0.55 mJ/cm^2, which was 2.5 times larger than the saturation fluence, and covered with the 1 mm binary mask. The corresponding calculated THz peak field was evaluated to be 143 kV/cm.

Following the same approach, Ropagnol et al. further improved the peak field strength of the emitted THz pulses by significantly increasing the surface area of the ILAPCA with an active surface of 4.4 cm^2 when covered by a shadow mask [34]. The interdigitated antenna structure consisted of 35 identical electrodes with an equally bright and dark gap size of 0.7 mm. The illuminated active area was 35% of the total area of the antenna. The whole antenna structure was covered by an Al_2O_3 encapsulation layer with a thickness of 300 nm, which also acts as an antireflection layer. The ILAPCA was illuminated using the second harmonic generation (SHG) of an amplified Ti:sapphire with up to 24 mJ pulse energy, operating at a repetition rate of 10 Hz. Despite this relatively low repetition rate of the laser, the signal-to-noise ratio of the detected electric field was relatively high, with an amplitude signal-to-noise ratio around 500 with only one scan. This value was possible because the pulsed bias voltage was set to be only half the repetition rate of the laser and acts like an electronic chopper [144]. The waveform of the THz pulses is a quasi-half cycle with a peak frequency located at 0.12 THz and the main frequency components below 1 THz (Fig. 21). The maximum energy of the THz pulses was found to be 8.3 μJ when the ILAPCA was covered by the shadow mask, biased at 42 kV/cm and excited with 15 mJ of optical energy. The corresponding calculated peak electric field was slightly above 0.3 MV/cm. Despite having a much higher THz pulse energy, this peak electric field strength is much lower than the peak intensity of the THz pulses emitted by the $LiNbO_3$ source with the pulse-front-tilt technique [145]. This is because the beam radius spot size was 1.17 and 1.37 mm in the X and Y direction, respectively. These dimensions are much large than a diffraction-limited spot size of a THz beam generated by a $LiNbO_3$ crystal. Despite this difference in the THz peak

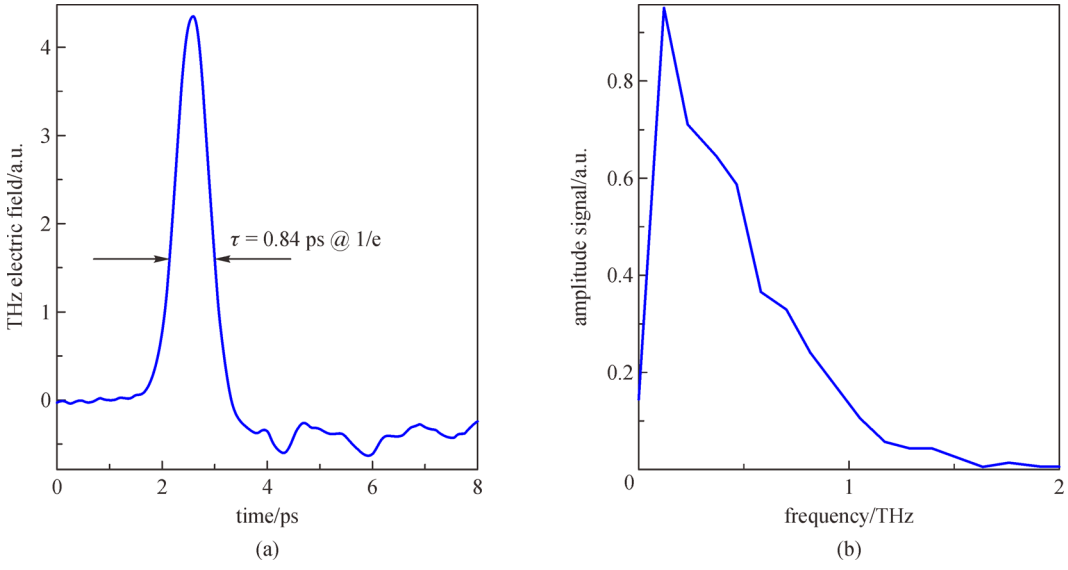

Fig. 21 THz waveform acquired by electro-optic sampling (EOS) of emission from ZnSe interdigitated LAPCA with Ti/Au contacts, using a shadow mask, excited with 16 mJ of 400 nm optical pump and biased with 30 kV/cm. (b) Respective amplitude THz spectrum [34]

electric field, in this specific case for this ILAPCA, the maximum ponderomotive energy of the THz pulses was calculated to be 15 eV, which is slightly higher than the ponderomotive energy of the THz pulses at 1 THz with an electric field of 1 MV/cm.

In pursuit of increasing the intensity of THz pulses generated by ILAPCAs, we can easily imagine that increasing the area of the ILAPCA structure is a straightforward solution. However, the multiplication of the number of electrodes inside the antennas array strongly increases the total capacitance of the ILAPCAs, which leads to a limitation of the maximum THz energy radiated in free space [127]. Also, the high voltage pulse was stretch and distorted, limiting the maximum bias field that could be applied before the appearance of corona discharges [116].

To verify the large ponderomotive potential of these THz pulses, the nonlinear transmission inside an n-doped InGaAs thin layer, deposited onto a semi-insulating InP substrate, was studied using an open aperture *Z*-scan technique. With a measured peak field of 174 kV/cm, a maximum transmission enhancement of 12.7 was observed at the focus of the THz pulse. This transmission enhancement is 4.5 times larger than the observed transmission enhancement inside the same InGaAs layer sample, obtained with a peak field of 200 kV/cm and a peak frequency located at 1.0 THz [34]. More importantly, it is shown that these THz pulses generated by the ZnSe ILAPCAs generated high-frequency components in the same n-doped InGaAs layer [146] (Fig. 22).

In another recent study, the performance of the ZnSe and 6H-SiC ILAPCAs covered by shadow masks were compared. The two ILAPCAs did not have the same interdigitated structure with a gap size of 0.8 and 1.0 mm for the ZnSe and the 6H-SiC ILAPCAs, respectively. However, the optical beam dimensions, the optical energy at 400 nm and the bias field were kept the same at 3.9 cm, 6.5 mJ and 30 kV/cm, respectively. A photo of the studied 6H-SiC ILAPCA is shown in Fig. 23. The THz pulses emitted by the ILAPCAs were detected by electro-optic sampling using a 0.3 mm (110) GaP crystal. With a peak electric field strength of 51 kV/cm, the 6H-SiC ILAPCA has exhibited slightly better performance than the peak field of the THz pulses generated by the ZnSe ILAPCA. As we can see in Fig. 24(a), the peak intensity of the emitted THz pulses from both antennas is observed at the same timing of 4 ps with a pulse duration (FWHM) of 590 fs. The major difference between the two pulses is in the negative tail, where we can observe strong oscillation of the electric field from THz pulses generated by the ZnSe ILAPCAs. Since the experiment has been done in both cases in the same unpurged environment, these oscillations are not from water. In reality, these oscillations are due to the fast variation of the photocurrent density in the ZnSe substrate. In the case of the 6H-SiC substrate, the decay of the photocurrent is probably smoother than that for the ZnSe crystal due to the indirect nature of the bandgap. In terms of spectra, both spectra have a peak frequency located around 100 GHz and extending up to 3.0 and 2.5 THz for the ZnSe and the 6H-SiC ILAPCAs, respectively. However, the spectra of the THz pulses generated by the ZnSe ILAPCA have its amplitude larger than the one of THz pulses generated by the 6H-SiC ILAPCA between 0.5 and 3 THz. This difference is attributed to the fast oscillation in the tail of the THz pulses generated by the ZnSe ILAPCA.

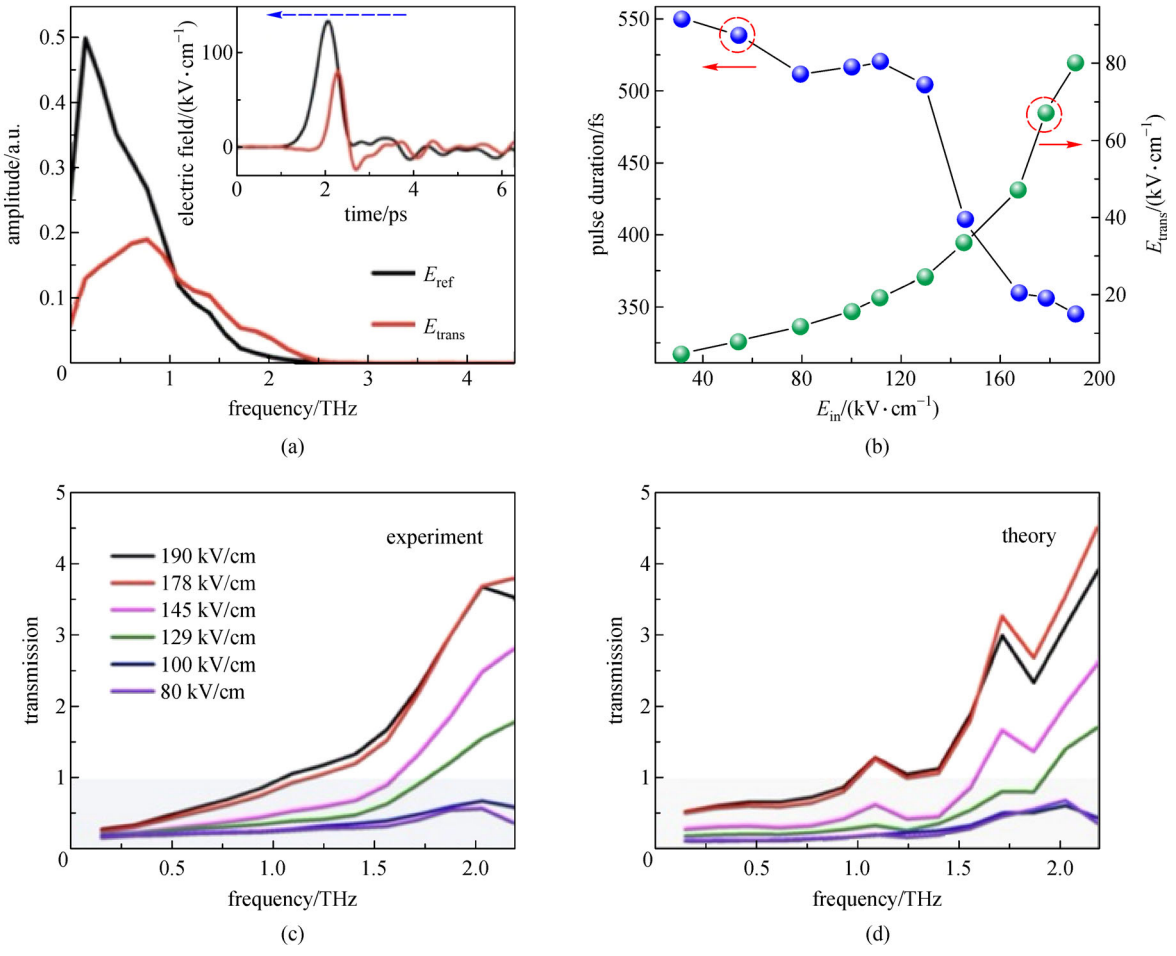

Fig. 22 (a) Amplitude of the transmitted THz pulses through the bare substrate (E_{ref}) and the InGaAs sample (E_{trans}) with the incident peak field of 190 kV/cm. Inset: corresponding terahertz waveforms, where the blue arrow indicates the propagation direction. (b) Measured field dependence of E_{trans} and half-cycle duration (amplitude FWHM) as a function of the incident peak field E_{in} measured in air. (c) Measured transmission spectra at various incident fields. The gray area corresponds to the transmission lower than 1. (d) Calculated transmission spectra based on the described model [146]

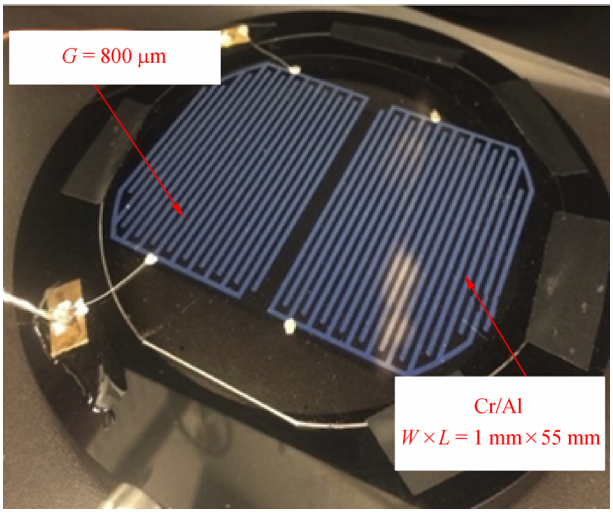

Fig. 23 Top view of a typical 6H-SiC ILAPCA. Here, the ILAPCA is composed of 38 electrodes with a gap size of 800 μm and a width and length of 1 and 55 mm respectively

3.3 6H-SiC and 4H-SiC LAPCAs excited by sub-picosecond UV lasers

As we described in Section 2, both 6H-SiC and 4H-SiC LAPCAs have shown good performance for generating intense THz pulses under UV laser excitation. To generate high-intensity THz pulses, two 6H-SiC and 4H-SiC ILAPCAs were fabricated, and their performances were studied under the excitation of a KrF excimer laser with a wavelength of 248 nm, a pulse duration of 0.7 ps and an energy of 80 mJ [35]. The antenna structure was simple and consisted of 18 electrodes with the same bright and dark gap size and the same electrode width of 1 mm. The total illuminated area was 4.5 cm^2. Since only a shadow mask is used in this experience, only 25% of the total area of the ILAPCA was illuminated (Fig. 25). The electrode composition was Cr/Al, and the end of the electrodes was circular to allow the largest bias field to be applied without surface flashovers occurring at the edges of the electrodes. As expected, when both ILAPCAs are excited with an optical fluence above the saturation fluence (1.2 mJ/cm^2),

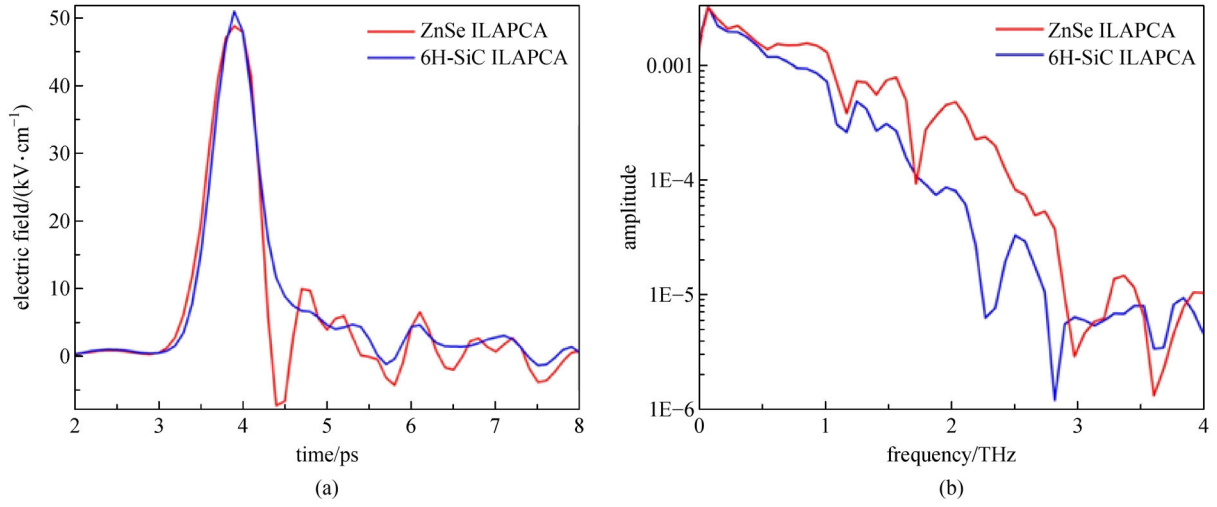

Fig. 24 (a) Peak electric field of the THz pulses emitted by ZnSe (purple) and 6H-SiC (red) ILAPCAs. (b) Power spectrum of 6H-SiC ILAPCA in frequency range

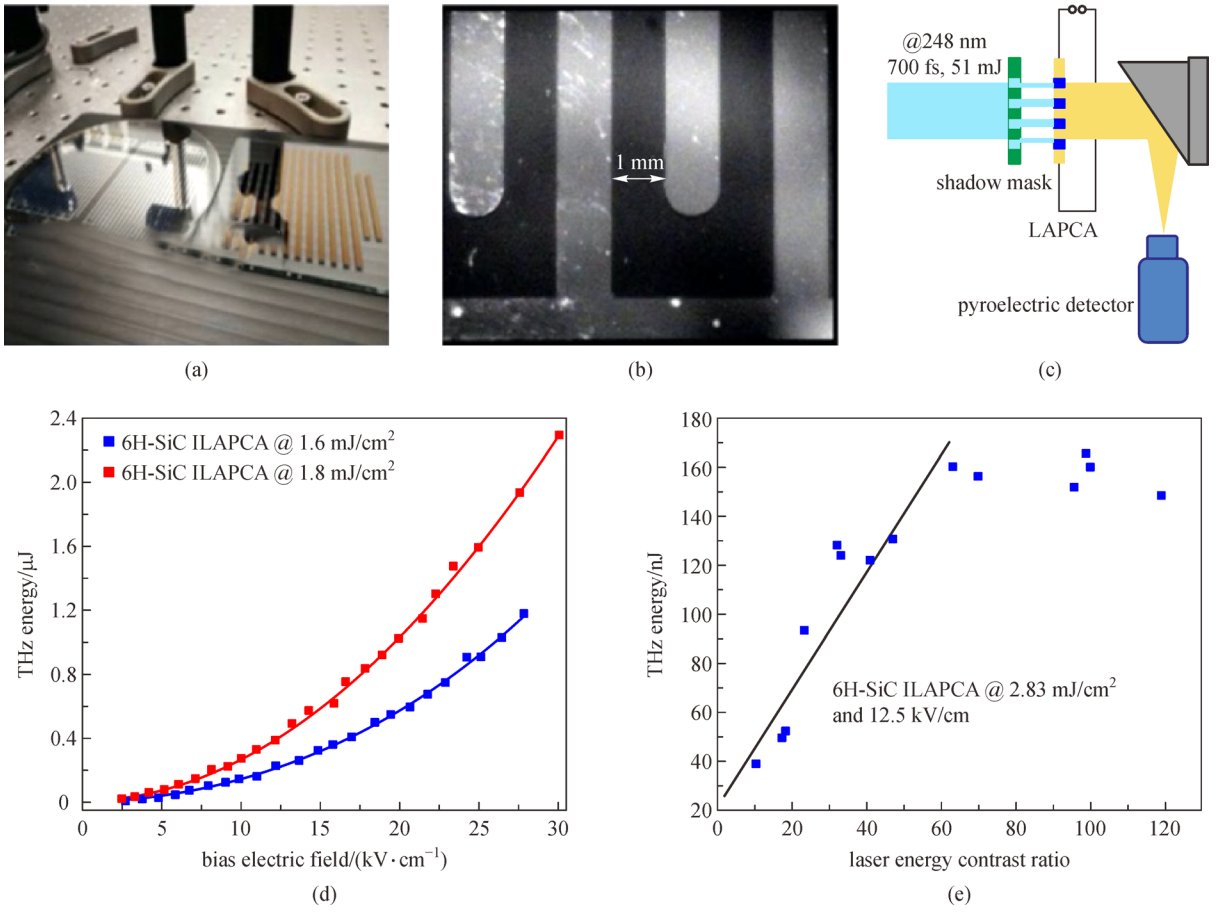

Fig. 25 (a) Photo of the structure of two ILAPCAS on a 4 inch diameter 6H-SiC wafer and the shadow mask. (b) Microscope image of the rounding edge of the ILAPCA structure on the 4H-SiC substrate. (c) Scheme of the experimental set-up. (d) Scaling of the THz energy as a function of the bias electric field for 6H-SiC and 4H-SiC ILAPCAs. And (e) scaling of the THz energy as a function of the laser energy contrast ratio for the 6H-SiC ILAPCA biased at 12.5 kV/cm and pumped with 2.83 mJ/cm^2 [35]

the 4H-SiC exhibits better overall performance than the 6H-SiC ILAPCA. The maximum energy of the THz pulses generated by the 4H-SiC ILAPCA was 2.3 μJ, with a bias field of 30 kV/cm. Using a Michelson interferometer, the measured FWHM of the half-cycle pulse was around 2.2 ps. This duration is approximately four times longer than the pulse duration of the THz pulses emitted by the ZnSe ILAPCA when excited at 400 nm laser beam with 50 fs duration. Consequently, the spectra of these THz pulses show a peak frequency located at 50 GHz with the cut-off frequency at 400 GHz. The latter can be described as sub-THz radiation. The main reason for this longer duration of THz pulses and these sub-THz frequencies is explained by the much longer duration of the laser pulse [88,107]. However, there is also the effect of the carrier dynamics inside the substrate with electrons being pumped into the satellite valley since the photon energy of the laser is much larger than the bandgap of the substrate [71,72,108,147]. By placing the 4H-SiC ILAPCA in a vacuum chamber, the maximum bias field was increased up to 64 kV/cm before the corona discharge occurred. In this condition and with optical energy of 54 mJ, the measured THz energy was 11 μJ, which is the highest THz pulse energy ever generated by ILAPCAs to date. The corresponding THz peak radiation field was calculated as 117 kV/cm. Although this peak field is relatively small, the associated ponderomotive energy was as large as 60 eV. Using these THz pulses with higher ponderomotive energy, an open Z-scan experiment was performed to demonstrate the nonlinear effect in the n-doped InGaAs layer. An increase in nonlinear transmission of 1.7 times was observed (Fig. 26). This transmission enhancement is relatively low, and we believe that the very high scattering rate of InGaAs limits the maximum kinetic energy that electrons can gain over the whole duration of the half-cycle pulse before they scatter into the satellite valley.

4 Conclusion and future perspectives

The current paper provides a general overview of the evolution and state-of-art of LAPCAs by gathering the past and recent achievements in the development and characterization of intense THz photoconductive emitters. Studies have shown that these emitters can generate high-intensity sub-cycle THz pulses with a central frequency ranging from several 10 s of GHz to a couple of 100 GHz with a relatively narrow spectrum and cutoff frequency below 2 THz. LAPCAs are very attractive and compact THz sources capable of operating at room temperature without cryogenic cooling and exhibit high optical-to-THz conversion efficiency while being pumped with relatively low optical power. Recent studies have shown that, compared to other sources, LAPCAs promise higher ponderomotive energy and high shot-to-shot pulse stability of the emitted THz pulses, which would pave the way toward the sensitive control of nonlinear optical effects in different materials. However, although the peak electric field of the emitted sub-cycle THz pulses can reach up to a few hundred kV/cm, there are still certain limiting factors of the THz PCA technology, such as the saturation of the emitted THz pulses with high optical pump powers and higher applied bias voltage limitation due to air breakdown. Several techniques have been discussed to overcome these limitations. For example, one can encapsulate the antenna electrodes with high resistivity epoxy to increase the bias voltage applied across the electrodes. Despite these latter limitations, generated

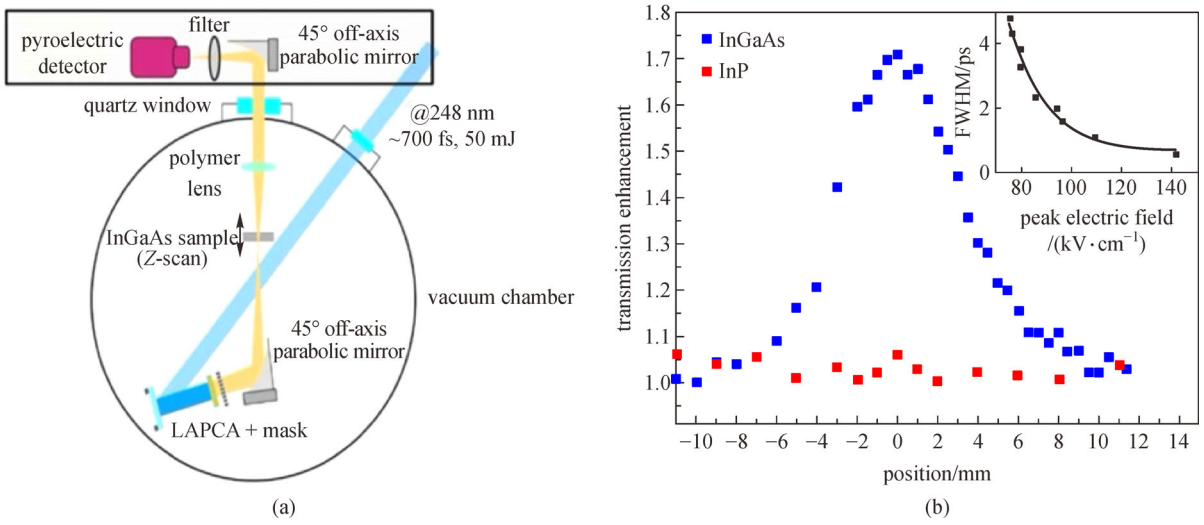

Fig. 26 (a) Experimental scheme of the *Z*-scan experiment with the InGaAs sample. (b) Normalized transmission as a function of the *Z*-scan position for the InGaAs sample and the InP substrate, with a THz pulse energy of 11 μJ. Inset shows the simulated results of the FWHM duration of the THz pulse as a function of the THz peak electric field for a transmission enhancement of 1.7 [35]

asymmetric high sub-cycle THz pulse intensities up to several hundred kV/cm have resulted in an increase in the associated ponderomotive energy as high as 60 eV in vacuum, which is considerably higher than that of THz pulses with a peak field strength of 1 MV/cm generated by $LiNbO_3$ sources. The unique properties of these low-frequency THz pulses with higher potential make them attractive for the study of various phenomena in nonlinear THz optics, such as carrier heating, impact ionization dynamics by inter-band and intra-band scatterings in the narrowband semiconductors at this frequency range. Another unique property of the LAPCA with interdigitated electrodes is that it allows the polarization control of the THz pulses radiated, which remains a challenge for other THz sources. In addition, recent work on LAPCAs shows that an applied external magnetic field can significantly increase the peak intensity of the THz pulses radiated in the far-field by overcoming the radiation screening effect, which is one of the main limitations of PCAs. All these performances mentioned above allow the LAPCAs to monitor carrier dynamics in semiconductors at the picosecond timescale, which extends the scope of THz photonics to a wide range of new applications to develop future electronic and optoelectronic devices.

References

1. Tonouchi M. Cutting-edge terahertz technology. Nature Photonics, 2007, 1: 97–105
2. Consolino L, Bartalini S, De Natale P. Terahertz frequency metrology for spectroscopic applications: a review. Journal of Infrared, Millimeter and Terahertz Waves, 2017, 38(11): 1289–1315
3. Nicoletti D, Cavalleri A. Nonlinear light–matter interaction at terahertz frequencies. Advances in Optics and Photonics, 2016, 8(3): 401
4. Fausti D, Tobey R I, Dean N, Kaiser S, Dienst A, Hoffmann M C, Pyon S, Takayama T, Takagi H, Cavalleri A. Light-induced superconductivity in a stripe-ordered cuprate. Science, 2011, 331(6014): 189–191
5. Först M, Tobey R I, Bromberger H, Wilkins S B, Khanna V, Caviglia A D, Chuang Y D, Lee W S, Schlotter W F, Turner J J, Minitti M P, Krupin O, Xu Z J, Wen J S, Gu G D, Dhesi S S, Cavalleri A, Hill J P. Melting of charge stripes in vibrationally driven $La_{1.875}Ba_{0.125}CuO_4$: assessing the respective roles of electronic and lattice order in frustrated superconductors. Physical Review Letters, 2014, 112(15): 157002
6. Mankowsky R, Subedi A, Först M, Mariager S O, Chollet M, Lemke H T, Robinson J S, Glownia J M, Minitti M P, Frano A, Fechner M, Spaldin N A, Loew T, Keimer B, Georges A, Cavalleri A. Nonlinear lattice dynamics as a basis for enhanced superconductivity in $YBa_2Cu_3O_{6.5}$. Nature, 2014, 516(7529): 71–73
7. Kaiser S, Clark S R, Nicoletti D, Cotugno G, Tobey R I, Dean N, Lupi S, Okamoto H, Hasegawa T, Jaksch D, Cavalleri A. Optical properties of a vibrationally modulated solid state Mott insulator. Scientific Reports, 2014, 4: 3823
8. Mitrano M, Cantaluppi A, Nicoletti D, Kaiser S, Perucchi A, Lupi S, Di Pietro P, Pontiroli D, Riccò M, Clark S R, Jaksch D, Cavalleri A. Possible light-induced superconductivity in K_3C_{60} at high temperature. Nature, 2016, 530(7591): 461–464
9. Zhang X C, Shkurinov A, Zhang Y. Extreme terahertz science. Nature Photonics, 2017, 11: 16–18
10. Matsunaga R, Tsuji N, Fujita H, Sugioka A, Makise K, Uzawa Y, Terai H, Wang Z, Aoki H, Shimano R. Light-induced collective pseudospin precession resonating with Higgs mode in a superconductor. Science, 2014, 345(6201): 1145–1149
11. Matsunaga R, Hamada Y I, Makise K, Uzawa Y, Terai H, Wang Z, Shimano R. Higgs amplitude mode in the BCS superconductors $Nb_{1-x}Ti_xN$ induced by terahertz pulse excitation. Physical Review Letters, 2013, 111(5): 057002
12. Rajasekaran S, Casandruc E, Laplace Y, Nicoletti D, Gu G D, Clark S R, Jaksch D, Cavalleri A. Parametric amplification of a superconducting plasma wave. Nature Physics, 2016, 12(11): 1012–1016
13. Auston D H, Cheung K P, Smith P R. Picosecond photoconducting Hertzian dipoles. Applied Physics Letters, 1984, 45(3): 284–286
14. Darrow J T, Zhang X C, Auston D H, Morse J D. Saturation properties of large-aperture photoconducting antennas. IEEE Journal of Quantum Electronics, 1992, 28(6): 1607–1616
15. Stone M R, Naftaly M, Miles R E, Fletcher J R, Steenson D P. Electrical and radiation characteristics of semilarge photoconductive terahertz emitters. IEEE Transactions on Microwave Theory and Techniques, 2004, 52(10): 2420–2429
16. Reid M, Fedosejevs R. Quantitative comparison of terahertz emission from (100) InAs surfaces and a GaAs large-aperture photoconductive switch at high fluences. Applied Optics, 2005, 44(1): 149–153
17. Grischkowsky D, Keiding S, van Exter M, Fattinger C. Far-infrared time-domain spectroscopy with terahertz beams of dielectrics and semiconductors. Journal of the Optical Society of America B, Optical Physics, 1990, 7(10): 2006
18. Hafez H A, Chai X, Ibrahim A, Mondal S, Férachou D, Ropagnol X, Ozaki T. Intense terahertz radiation and their applications. Journal of Optics, 2016, 18(9): 093004
19. Ulbricht R, Hendry E, Shan J, Heinz T F, Bonn M. Carrier dynamics in semiconductors studied with time-resolved terahertz spectroscopy. Reviews of Modern Physics, 2011, 83(2): 543–586
20. Pačebutas V, Bičiūnas A, Balakauskas S, Krotkus A, Andriukaitis G, Lorenc D, Pugžlys A, Baltuška A. Terahertz time-domain-spectroscopy system based on femtosecond Yb:fiber laser and GaBiAs photoconducting component. Applied Physics Letters, 2010, 97(3): 031111
21. Rungsawang R, Ohta K, Tukamoto K, Hattori T. Ring formation of focused half-cycle terahertz pulses. Journal of Physics D, Applied Physics, 2003, 36(3): 229
22. Razzari L, Su F H, Sharma G, Blanchard F, Ayesheshim A, Bandulet H C, Morandotti R, Kieffer J C, Ozaki T, Reid M, Hegmann F A. Nonlinear ultrafast modulation of the optical absorption of intense few-cycle terahertz pulses in n-doped semiconductors. Physical Review B: Condensed Matter and Materials Physics, 2009, 79(19): 193204

23. Hu B B, Nuss M C. Imaging with terahertz waves. Optics Letters, 1995, 20(16): 1716
24. Mittleman D M, Gupta M, Neelamani R, Baraniuk R G, Rudd J V, Koch M. Recent advances in terahertz imaging. Applied Physics B, Lasers and Optics, 1999, 68(6): 1085–1094
25. Jiang Z, Zhang X C. Single-shot spatiotemporal terahertz field imaging. Optics Letters, 1998, 23(14): 1114–1116
26. O'Hara J, Grischkowsky D. Quasi-optic terahertz imaging. Optics Letters, 2001, 26(23): 1918–1920
27. Zeitler J A, Gladden L F. *In-vitro* tomography and non-destructive imaging at depth of pharmaceutical solid dosage forms. European Journal of Pharmaceutics and Biopharmaceutics, 2009, 71(1): 2–22
28. Jepsen P U, Cooke D G, Koch M. Terahertz spectroscopy and imaging-modern techniques and applications. Laser & Photonics Reviews, 2011, 5(1): 124–166
29. Yang S H, Hashemi M R, Berry C W, Jarrahi M. 7.5% optical-to-terahertz conversion efficiency offered by photoconductive emitters with three-dimensional plasmonic contact electrodes. IEEE Transactions on Terahertz Science and Technology, 2014, 4 (5): 575–581
30. Yardimci N T, Lu H, Jarrahi M. High power telecommunication-compatible photoconductive terahertz emitters based on plasmonic nano-antenna arrays. Applied Physics Letters, 2016, 109(19): 191103
31. Yardimci N T, Cakmakyapan S, Hemmati S, Jarrahi M. Significant efficiency enhancement in photoconductive terahertz emitters through three-dimensional light confinement. In: Proceedings of IEEE MTT-S International Microwave Symposium. Honololu: IEEE, 2017, 435–438
32. Yardimci N T, Cakmakyapan S, Hemmati S, Jarrahi M. A high-power broadband terahertz source enabled by three-dimensional light confinement in a plasmonic nanocavity. Scientific Reports, 2017, 7(1): 4166
33. Jones R R, You D, Bucksbaum P H. Ionization of Rydberg atoms by subpicosecond half-cycle electromagnetic pulses. Physical Review Letters, 1993, 70(9): 1236–1239
34. Ropagnol X, Khorasaninejad M, Raeiszadeh M, Safavi-Naeini S, Bouvier M, Côté C Y, Laramée A, Reid M, Gauthier M A, Ozaki T. Intense THz pulses with large ponderomotive potential generated from large aperture photoconductive antennas. Optics Express, 2016, 24(11): 11299–11311
35. Ropagnol X, Kovács Z, Gilicze B, Zhuldybina M, Blanchard F, Garcia-Rosas C M, Szatmári S, Földes I B, Ozaki T. Intense sub-terahertz radiation from wide-bandgap semiconductor based large-aperture photoconductive antennas pumped by UV lasers. New Journal of Physics, 2019, 21(11): 113042
36. Fülöp J A, Tzortzakis S, Kampfrath T. Laser-driven strong-field terahertz sources. Advanced Optical Materials, 2020, 8(3): 1900681
37. Kampfrath T, Tanaka K, Nelson K A. Resonant and nonresonant control over matter and light by intense terahertz transients. Nature Photonics, 2013, 7: 680–690
38. Ropagnol X, Morandotti R, Ozaki T, Reid M. THz pulse shaping and improved optical-to-THz conversion efficiency using a binary phase mask. Optics Letters, 2011, 36(14): 2662–2664
39. You D, Dykaar D R, Jones R R, Bucksbaum P H. Generation of high-power sub-single-cycle 500-fs electromagnetic pulses. Optics Letters, 1993, 18(4): 290
40. Brown E R, Smith F W, McIntosh K A. Coherent millimeter-wave generation by heterodyne conversion in low-temperature-grown GaAs photoconductors. Journal of Applied Physics, 1993, 73(3): 1480–1484
41. Emadi R, Barani N, Safian R, Nezhad A Z. Hybrid computational simulation and study of terahertz pulsed photoconductive antennas. Journal of Infrared, Millimeter and Terahertz Waves, 2016, 37 (11): 1069–1085
42. Kim D S, Citrin D S. Coulomb and radiation screening in photoconductive terahertz sources. Applied Physics Letters, 2006, 88(16): 161117
43. Tiedje H F, Saeedkia D, Nagel M, Haugen H K. Optical scanning techniques for characterization of terahertz photoconductive antenna arrays. In: Proceedings of the 33rd International Conference on Infrared and Millimeter Waves and the 16th International Conference on Terahertz Electronics. Pasadena: IEEE, 2008, 1–2
44. Hou L, Shi W. An LT-GaAs terahertz photoconductive antenna with high emission power, low noise, and good stability. IEEE Transactions on Electron Devices, 2013, 60(5): 1619–1624
45. Huang Y, Khiabani N, Shen Y, Li D. Terahertz photoconductive antenna efficiency. In: Proceedings of 2011 International Workshop on Antenna Technology (iWAT). Hong Kong: IEEE, 2011, 152–156
46. Burford N M, El-Shenawee M O. Review of terahertz photoconductive antenna technology. Optical Engineering (Redondo Beach, Calif.), 2017, 56(1): 010901
47. Tani M, Matsuura S, Sakai K, Nakashima S. Emission characteristics of photoconductive antennas based on low-temperature-grown GaAs and semi-insulating GaAs. Applied Optics, 1997, 36 (30): 7853–7859
48. Tani M, Yamamoto K, Estacio E S, Que C T, Nakajima H, Hibi M, Miyamaru F, Nishizawa S, Hangyo M. Photoconductive emission and detection of terahertz pulsed radiation using semiconductors and semiconductor devices. Journal of Infrared, Millimeter and Terahertz Waves, 2012, 33(4): 393–404
49. Shi W, Hou L, Wang X. High effective terahertz radiation from semi-insulating-GaAs photoconductive antennas with ohmic contact electrodes. Journal of Applied Physics, 2011, 110(2): 023111
50. Benicewicz P K, Taylor A J. Scaling of terahertz radiation from large-aperture biased InP photoconductors. Optics Letters, 1993, 18(16): 1332
51. Ropagnol X, Morandotti R, Ozaki T, Reid M. Toward high-power terahertz emitters using large aperture ZnSe photoconductive antennas. IEEE Photonics Journal, 2011, 3(2): 174–186
52. Prajapati J, Bharadwaj M, Chatterjee A, Bhattacharjee R. Magnetic field-assisted radiation enhancement from a large aperture photoconductive antenna. IEEE Transactions on Microwave Theory and Techniques, 2018, 66(2): 678–687
53. Ropagnol X. Développement d'une source de radiation terahertz (THz) intense et mise en forme d'impulsions THz àpartir d'une antenne de grande ouverture de ZnSe. 2013

54. Wang X, Shi W, Hou L, Ma D, Qu G. Investigation of semi-insulating gallium arsenide photoconductive photodetectors. In: Proceedings of 2008 International Conference on Optical Instruments and Technology: Advanced Sensor Technologies and Applications. Beijing: SPIE, 2008, 71570B
55. Yoneda H, Tokuyama K, Ueda K, Yamamoto H, Baba K. High-power terahertz radiation emitter with a diamond photoconductive switch array. Applied Optics, 2001, 40(36): 6733–6736
56. Meng P, Zhao X, Yang X, Wu J, Xie Q, He J, Hu J, He J. Breakdown phenomenon of ZnO varistors caused by non-uniform distribution of internal pores. Journal of the European Ceramic Society, 2019, 39(15): 4824–4830
57. Singh B P, Imafuji O, Hirose Y, Fukushima Y, Takigawa S, Ueda D. High power C-doped GaN photoconductive THz emitter. In: Proceedings of Joint 32nd International Conference on Infrared and Millimetre Waves, and 15th International Conference on Terahertz Electronics. Cardiff: IEEE, 2007, 1004–1005
58. Ropagnol X, Morandotti R, Ozaki T, Reid M. Towards high-power terahertz emitters using large aperture ZnSe photoconductive antennas. In: Proceedings of Laser Science to Photonic Applications. San Jose: IEEE, 2010, 1–2
59. Doğan S, Teke A, Huang D, Morkoç H, Roberts C B, Parish J, Ganguly B, Smith M, Myers R E, Saddow S E. 4H-SiC photoconductive switching devices for use in high-power applications. Applied Physics Letters, 2003, 82(18): 3107–3109
60. Friedrichs P, Burte E P, Schörner R. Dielectric strength of thermal oxides on 6H-SiC and 4H-SiC. Applied Physics Letters, 1994, 65 (13): 1665–1667
61. Imafuji O, Singh B P, Hirose Y, Fukushima Y, Takigawa S. High power subterahertz electromagnetic wave radiation from GaN photoconductive switch. Applied Physics Letters, 2007, 91(7): 071112
62. Wang L M. Relationship between intrinsic breakdown field and bandgap of materials. In: Proceedings of the 25th International Conference on Microelectronics. Belgrade: IEEE, 2006, 615–618
63. Ropagnol X, Bouvier M, Reid M, Ozaki T. Improvement in thermal barriers to intense terahertz generation from photoconductive antennas. Journal of Applied Physics, 2014, 116(4): 043107
64. Hou L, Shi W, Chen S. Noise analysis and optimization of terahertz photoconductive emitters. IEEE Journal of Selected Topics in Quantum Electronics, 2013, 19(1): 8401305
65. Moreno E, Pantoja M F, Ruiz F G, Roldán J B, García S G. On the numerical modeling of terahertz photoconductive antennas. Journal of Infrared, Millimeter and Terahertz Waves, 2014, 35 (5): 432–444
66. Castro-Camus E, Fu L, Lloyd-Hughes J, Tan H H, Jagadish C, Johnston M B. Photoconductive response correction for detectors of terahertz radiation. Journal of Applied Physics, 2008, 104(5): 053113
67. Park S G, Weiner A M, Melloch M R, Siders C W, Siders J L W, Taylor A J. High-power narrow-band terahertz generation using large-aperture photoconductors. IEEE Journal of Quantum Electronics, 1999, 35(8): 1257–1268
68. Benicewicz P K, Roberts J P, Taylor A J. Scaling of terahertz radiation from large-aperture biased photoconductors. Journal of the Optical Society of America B, Optical Physics, 1994, 11(12): 2533
69. Duvillaret L, Garet F, Roux J F, Coutaz J L. Analytical modeling and optimization of terahertz time-domain spectroscopy experiments using photoswitches as antennas. IEEE Journal of Selected Topics in Quantum Electronics, 2001, 7(4): 615–623
70. Castro-Camus E, Lloyd-Hughes J, Johnston M B. Three-dimensional carrier-dynamics simulation of terahertz emission from photoconductive switches. Physical Review B: Condensed Matter and Materials Physics, 2005, 71(19): 195301
71. Prajapati J, Bharadwaj M, Chatterjee A, Bhattacharjee R. Radiation field analysis of a photoconductive antenna using an improved carrier dynamics. Semiconductor Science and Technology, 2019, 34(2): 024004
72. Piao Z, Tani M, Sakai K. Carrier dynamics and terahertz radiation in photoconductive antennas. Japanese Journal of Applied Physics, 2000, 39(1): 96–100
73. Winnerl S, Peter F, Nitsche S, Dreyhaupt A, Zimmermann B, Wagner M, Schneider H, Helm M, Köhler K. Generation and detection of THz radiation with scalable antennas based on GaAs substrates with different carrier lifetimes. IEEE Journal of Selected Topics in Quantum Electronics, 2008, 14(2): 449–457
74. Shi W, Sun X F, Zeng J, Jia W L. Carrier dynamics and terahertz radiation in large-aperture photoconductive antenna. In: Proceedings of International Symposium on Photoelectronic Detection and Imaging 2007: Laser, Ultraviolet, and Terahertz Technology. Beijing: SPIE, 2008, 662228
75. Liu D, Qin J. Carrier dynamics of terahertz emission from low-temperature-grown GaAs. Applied Optics, 2003, 42(18): 3678–3683
76. Piao Z, Tani M, Sakai K. Carrier dynamics and THz radiation in biased semiconductor structures. In: Proceedings of SPIE 3617, Terahertz Spectroscopy and Applications. San Jose: SPIE, 1999, 49–56
77. Chen L, Fan W. Numerical simulation of terahertz generation and detection based on ultrafast photoconductive antennas. In: Proceedings of International Symposium on Photoelectronic Detection and Imaging 2011: Terahertz Wave Technologies and Applications. Beijing: SPIE, 2011, 81950K
78. Šlekas G, Kancleris Ž, Urbanowicz A, Čiegis R. Comparison of full-wave models of terahertz photoconductive antenna based on ordinary differential equation and Monte Carlo method. European Physical Journal Plus, 2020, 135(1): 85
79. Cadilhon B, Cassany B, Modin P, Diot J C, Bertrand V, Pecastaing L. Ultra Wideband Antennas for High Pulsed Power Applications. In: Matin M, ed. Ultra Wideband Communications: Novel Trends–Antennas and Propagation. Rijeka: InTech, 2011
80. Mahadevan S, Hardas S M, Suryan G. Electrical breakdown in semiconductors. Physica Status Solidi (a), 1971, 8(2): 335–374
81. Xu M, Li M, Shi W, Ma C, Zhang Q, Fan L, Shang X, Xue P. Temperature-dependence of high-gain operation in GaAs photoconductive semiconductor switch at 1.6 μJ excitation. IEEE Electron Device Letters, 2016, 37(1): 67–69
82. Qadri S B, Wu D H, Graber B D, Mahadik N A, Garzarella A. Failure mechanism of THz GaAs photoconductive antenna. Applied Physics Letters, 2012, 101(1): 011910
83. Sun C, Zhang A. Efficient terahertz generation from lightly ion-

beam-treated semi-insulating GaAs photoconductive antennas. Applied Physics Express, 2017, 10(10): 102202
84. Gupta S, Frankel M Y, Valdmanis J A, Whitaker J F, Mourou G A, Smith F W, Calawa A R. Subpicosecond carrier lifetime in GaAs grown by molecular beam epitaxy at low temperatures. Applied Physics Letters, 1991, 59(25): 3276–3278
85. Liu T A, Tani M, Nakajima M, Hangyo M, Pan C L. Ultrabroadband terahertz field detection by photoconductive antennas based on multi-energy arsenic-ion-implanted GaAs and semi-insulating GaAs. Applied Physics Letters, 2003, 83(7): 1322–1324
86. Salem B, Morris D, Aimez V, Beerens J, Beauvais J, Houde D. Pulsed photoconductive antenna terahertz sources made on ion-implanted GaAs substrates. Journal of Physics Condensed Matter, 2005, 17(46): 7327
87. Salem B, Morris D, Salissou Y, Aimez V, Charlebois S, Chicoine M, Schiettekatte F. Terahertz emission properties of arsenic and oxygen ion-implanted GaAs based photoconductive pulsed sources. Journal of Vacuum Science & Technology A, Vacuum, Surfaces, and Films, 2006, 24(3): 774–777
88. Ono S, Murakami H, Quema A, Diwa G, Sarukura N, Nagasaka R, Ichikawa Y, Ogino H, Ohshima E, Yoshikawa A, Fukuda T. Generation of terahertz radiation using zinc oxide as photoconductive material excited by ultraviolet pulses. Applied Physics Letters, 2005, 87(26): 261112
89. Beck M, Schäfer H, Klatt G, Demsar J, Winnerl S, Helm M, Dekorsy T. Impulsive terahertz radiation with high electric fields from an amplifier-driven large-area photoconductive antenna. Optics Express, 2010, 18(9): 9251–9257
90. Gavrushchuk E M. Polycrystalline zinc selenide for IR optical applications. Inorganic Materials, 2003, 39(9): 883–899
91. Cho P S, Peng F, Ho P T, Goldhar J, Lee C H. ZnSe photoconductive switches with transparent electrodes. In: Proceedings of the 8th IEEE International Conference on Pulsed Power. San Diego: IEEE, 2005, 209–212
92. Ho P T, Peng F, Goldhar J. Photoconductive switching using polycrystalline ZnSe. IEEE Transactions on Electron Devices, 1990, 37(12): 2517–2519
93. Cho P S, Goldhar J, Lee C H, Saddow S E, Neudeck P. Photoconductive and photovoltaic response of high-dark-resistivity 6H-SiC devices. Journal of Applied Physics, 1995, 77(4): 1591–1599
94. Holzman J F, Elezzabi A Y. Two-photon photoconductive terahertz generation in ZnSe. Applied Physics Letters, 2003, 83 (14): 2967–2969
95. Mauch D, Sullivan W, Bullick A, Neuber A, Dickens J. High power lateral silicon carbide photoconductive semiconductor switches and investigation of degradation mechanisms. IEEE Transactions on Plasma Science, 2015, 43(6): 2021–2031
96. Shimizu H, Watanabe N, Morikawa T, Shima A, Iwamuro N. 1.2 kV silicon carbide Schottky barrier diode embedded MOSFETs with extension structure and titanium-based single contact. Japanese Journal of Applied Physics, 2020, 59(2): 026502
97. Kimoto T, Yonezawa Y. Current status and perspectives of ultrahigh-voltage SiC power devices. Materials Science in Semiconductor Processing, 2018, 78: 43–56
98. Bhalla A. Status of SiC Products and Technology. In: Sharma Y, ed. Disruptive Wide Bandgap Semiconductors, Related Technologies, and Their Applications. London: InTech, 2018
99. Xiao L, Yang X, Duan P, Xu H, Chen X, Hu X, Peng Y, Xu X. Effect of electron avalanche breakdown on a high-purity semi-insulating 4H-SiC photoconductive semiconductor switch under intrinsic absorption. Applied Optics, 2018, 57(11): 2804–2808
100. Yu D, Kang J, Berakdar J, Jia C. Nondestructive ultrafast steering of a magnetic vortex by terahertz pulses. NPG Asia Materials, 2020, 12(1): 36
101. Elliott D. Ultraviolet Laser Technology and Applications. New York: Academic Press, 2014
102. Duarte F. Tunable Lasers Handbook. New York: Academic Press,1996
103. Szatmári S, Rácz B, Schäffer F P. Bandwidth limited amplification of 220 fs pulses in XeCl. Optics Communications, 1987, 62(4): 271–276
104. Dick B, Szatmári S, Rácz B, Schäfer F P. Bandwidth limited amplification of 220 fs pulses in XeCl: theoretical and experimental study of temporal and spectral behavior. Optics Communications, 1987, 62(4): 277–283
105. Szatmári S, Schäfer F P, Müller-Horsche E, Müchenheim W. Hybrid dye-excimer laser system for the generation of 80 fs, 900 GW pulses at 248 nm. Optics Communications, 1987, 63(5): 305–309
106. Di G, Bhattacharya A, Samad S, Nayak B, Shah A P, Rahman A A, Bhattacharya A, Prabhu S S. Towards bandwidth-enhanced GaN-based terahertz photoconductive antennas. In: Proceedings of the 44th International Conference on Infrared, Millimeter, and Terahertz Waves. Paris: IEEE, 2019, 1–2
107. Szatmári S. High-brightness ultraviolet excimer lasers. Applied Physics B: Laser and Optics, 1994, 58(3): 211–223
108. Loata G C, Thomson M D, Löffler T, Roskos H G. Radiation field screening in photoconductive antennae studied via pulsed terahertz emission spectroscopy. Applied Physics Letters, 2007, 91(23): 232506
109. Budiarto E, Margolies J, Jeong S, Son J, Bokor J. High-intensity terahertz pulses at 1-kHz repetition rate. IEEE Journal of Quantum Electronics, 1996, 32(10): 1839–1846
110. Welsh G H, Turton D A, Jones D R, Jaroszynski D A, Wynne K. 200 ns pulse high-voltage supply for terahertz field emission. Review of Scientific Instruments, 2007, 78(4): 043103
111. Winnerl S, Zimmermann B, Peter F, Schneider H, Helm M. Terahertz Bessel-Gauss beams of radial and azimuthal polarization from microstructured photoconductive antennas. Optics Express, 2009, 17(3): 1571–1576
112. Cliffe M J, Rodak A, Graham D M, Jamison S P. Generation of longitudinally polarized terahertz pulses with field amplitudes exceeding 2 kV/cm. Applied Physics Letters, 2014, 105(19): 191112
113. .,Mourou G A, Bloom D M, Lee C H. Picosecond electronics and optoelectronics. In: Proceedings of the Topical Meeting Lake Tahoe. Nevada: SPIE, 1985, 438
114. Cox C H III, Diadiuk V, Yao I, Leonberger F J, Williamson R C. InP optoelectronic switches and their high-speed signal-processiny applications. In: Proceedings of Picosecond Optoelectronics. San

Diego: SPIE, 1983, 164–168
115. Hattori T, Egawa K, Ookuma S I, Itatani T. Intense terahertz pulses from large-aperture antenna with interdigitated electrodes. Japanese Journal of Applied Physics, 2006, 45(15): L422–L424
116. Chou S Y, Liu Y, Fischer P B. Tera-hertz GaAs metal-semiconductor-metal photodetectors with 25 nm finger spacing and finger width. Applied Physics Letters, 1992, 61(4): 477–479
117. Awad M, Nagel M, Kurz H, Herfort J, Ploog K. Characterization of low temperature GaAs antenna array terahertz emitters. Applied Physics Letters, 2007, 91(18): 181124
118. Acuna G, Buersgens F, Lang C, Handloser M, Guggenmos A, Kersting R. Interdigitated terahertz emitters. Electronics Letters, 2008, 44(3): 229–231
119. Ropagnol X, Blanchard F, Ozaki T, Reid M. Intense terahertz generation at low frequencies using an interdigitated ZnSe large aperture photoconductive antenna. Applied Physics Letters, 2013, 103(16): 161108
120. Dreyhaupt A, Winnerl S, Dekorsy T, Helm M. High-intensity terahertz radiation from a microstructured large-area photoconductor. Applied Physics Letters, 2005, 86(12): 121114
121. Go D B, Pohlman D A. A mathematical model of the modified Paschen's curve for breakdown in microscale gaps. Journal of Applied Physics, 2010, 107(10): 103303
122. Headley C, Fu L, Member S, Parkinson P, Xu X, Lloyd-Hughes J, Jagadish C, Johnston M B. Improved performance of GaAs-based terahertz emitters via surface passivation and silicon nitride encapsulation. IEEE Journal of Selected Topics in Quantum Electronics, 2011, 17(1): 17–21
123. Gupta A, Rana G, Bhattacharya A, Singh A, Jain R, Bapat R D, Duttagupta S P, Prabhu S S. Enhanced optical-to-THz conversion efficiency of photoconductive antenna using dielectric nano-layer encapsulation. APL Photonics, 2018, 3(5): 051706
124. Kirawanich P, Yakura S J, Islam N E. Study of high-power wideband terahertz-pulse generation using integrated high-speed photoconductive semiconductor switches. IEEE Transactions on Plasma Science, 2009, 37(1): 219–228
125. Singh A, Welsch M, Winnerl S, Helm M, Schneider H. Improved electrode design for interdigitated large-area photoconductive terahertz emitters. Optics Express, 2019, 27(9): 13108–13115
126. Ropagnol X, Chai X, Raeis-Zadeh S M, Safavi-Naeini S, Kirouac-Turmel M, Bouvier M, Cote C Y, Reid M, Gauthier M A, Ozaki T. Influence of gap size on intense THz generation from ZnSe interdigitated large aperture photoconductive antennas. IEEE Journal of Selected Topics in Quantum Electronics, 2017, 23(4): 1–8
127. Berry C W, Jarrahi M. Principles of impedance matching in photoconductive antennas. Journal of Infrared, Millimeter and Terahertz Waves, 2012, 33(12): 1182–1189
128. Emadi R, Safian R, Nezhad A Z. Theoretical modeling of terahertz pulsed photoconductive antennas based on hot-carriers effect. IEEE Journal of Selected Topics in Quantum Electronics, 2017, 23 (4): 1–9
129. Brown E R, McIntosh K A, Smith F W, Nichols K B, Manfra M J, Dennis C L, Mattia J P. Milliwatt output levels and superquadratic bias dependence in a low-temperature-grown GaAs photomixer. Applied Physics Letters, 1994, 64(24): 3311–3313
130. Ropagnol X, Blanchard F, Ozaki T, Reid M. Intense terahertz generation at low frequencies using an interdigitated ZnSe large aperture photoconductive antenna. Applied Physics Letters, 2013, 103(16): 161108
131. Bacon D R, Gill T B, Rosamond M, Burnett A D, Dunn A, Li L, Linfield E H, Davies A G, Dean P, Freeman J R. Photoconductive arrays on insulating substrates for high-field terahertz generation. Optics Express, 2020, 28(12): 17219–17231
132. Dreyhaupt A, Peter F, Winnerl S, Nitsche S, Wagner M, Schneider H, Helm M, Köhler K. Leistungsstarke emitter und einfach handhabbare detektoren für die terahertz-time-domain-spektroskopie. Technisches Messen., 2008, 75(1): 3–13
133. Winnerl S. Scalable microstructured photoconductive terahertz emitters. Journal of Infrared, Millimeter and Terahertz Waves, 2012, 33(4): 431–454
134. Matthäus G, Nolte S, Hohmuth R, Voitsch M, Richter W, Pradarutti B, Riehemann S, Notni G, Tünnermann A. Large-area microlens emitters for powerful THz emission. Applied Physics B, Lasers and Optics, 2009, 96(2–3): 233–235
135. Singh A, Prabhu S S. Microlensless interdigitated photoconductive terahertz emitters. Optics Express, 2015, 23(2): 1529–1535
136. Bacon D R, Gill T B, Rosamond M, Burnett A D, Dunn A, Li L, Linfield E H, Davies A G, Dean P, Freeman J R. Photoconductive arrays on insulating substrates for high-field terahertz generation. Optics Express, 2020, 28(12): 17219–17231
137. Singh A, Winnerl S, König-Otto J C, Stephan D R, Helm M, Schneider H. Plasmonic efficiency enhancement at the anode of strip line photoconductive terahertz emitters. Optics Express, 2016, 24(20): 22628–22634
138. Zhang X C. Generation and detection of terahertz electromagnetic pulses from semiconductors with femtosecond optics. Journal of Luminescence, 1995, 66–67(1–6): 488–492
139. Preu S, Dhler G H, Malzer S, Wang L J, Gossard A C. Tunable, continuous-wave terahertz photomixer sources and applications. Journal of Applied Physics, 2011, 109(6): 061301
140. Hale P J, Madeo J, Chin C, Dhillon S S, Mangeney J, Tignon J, Dani K M. 20 THz broadband generation using semi-insulating GaAs interdigitated photoconductive antennas. Optics Express, 2014, 22(21): 26358–26364
141. Madéo J, Jukam N, Oustinov D, Rosticher M, Rungsawang R, Tignon J, Dhillon S S. Frequency tunable terahertz interdigitated photoconductive antennas. Electronics Letters, 2010, 46(9): 611–613
142. Yardimci N T, Yang S H, Berry C W, Jarrahi M. High-power terahertz generation using large-area plasmonic photoconductive emitters. IEEE Transactions on Terahertz Science and Technology, 2015, 5(2): 223–229
143. Maussang K, Palomo J, Mangeney J, Dhillon S S, Tignon J. Large-area photoconductive switches as emitters of terahertz pulses with fully electrically controlled linear polarization. Optics Express, 2019, 27(10): 14784–14797
144. Sterczewski L A, Grzelczak M P, Plinski E F. Terahertz antenna electronic chopper. Review of Scientific Instruments, 2016, 87(1): 014702
145. Hirori H, Doi A, Blanchard F, Tanaka K. Single-cycle terahertz pulses with amplitudes exceeding 1 MV/cm generated by optical

rectification in $LiNbO_3$. Applied Physics Letters, 2011, 98(9): 091106

146. Chai X, Ropagnol X, Raeis-Zadeh S M, Reid M, Safavi-Naeini S, Ozaki T. Subcycle terahertz nonlinear optics. Physical Review Letters, 2018, 121(14): 143901
147. Moreno E, Pantoja M F, Ruiz F G, Roldán J B, García S G. On the numerical modeling of terahertz photoconductive antennas. Journal of Infrared, Millimeter and Terahertz Waves, 2014, 35 (5): 432–444

Elchin Isgandarov is a Ph.D. student at Institut National de la Recherche Scientifique Centre Énergie, Matériaux et Télécommunications (INRS-EMT), Canada. He received his B.Sc. and M.Sc. degrees in Physics and Semiconductor Physics respectively from Azerbaijan State Pedagogical University, Baku, Azerbaijan. He also obtained an M.Sc. degree in Nanophysics from University of Montpellier, France. His current research focuses on fabrication and development of intense THz large aperture photoconductive antennas (LAPCAs) and their application in the nonlinear THz time-domain spectroscopy.

Xavier Ropagnol graduated from University of Rouen, France in 2004 and received his M.Sc. degree from Rouen University in 2006 and his Ph.D. degree from Institut National de la Recherche Scientifique Centre Énergie, Matériaux et Télécommunications (INRS-EMT) in Varennes, Qc, Canada in 2013 with very good mention. During his PhD, he worked on the development of table top intense THz sources from large aperture photoconductive antenna and optical rectification. He also worked on the non-linear interaction of these THz pulses with matter with a particular attention on n-doped thin film semiconductor. From 2013 to 2014, he was post-doctoral student at McGill University, Montreal, Qc, Canada and at University of Northern British Columbia, Prince Georges, BC, Canada where he keeps working on intense THz sources and especially with wide bandgap semiconductor photoconductive antennas. He came back to Montreal in 2014 as a research associate at INRS-EMT and ÉTS, Montreal, Qc, Canada, where he is developing THz measurement tools such the THz chemical microscope and the THz imaging. In parallel, he is still developing THz sources and detector which are more adapted to ytterbium laser at wavelength of 1.03 μm. Today, his main research interests include high intensity THz radiations and their applications with matters, non-linear optics and development of THz technology for industrial environment.

Mangaljit Singh is a Ph.D. student at Institut National de la Recherche Scientifique Centre Énergie, Matériaux et Télécommunications (INRS-EMT), Canada. He received his Master degree in Applied Optics from Indian Institute of Technology, India. He is currently involved in studying the high-intensity ultrafast laser-matter interaction, particularly the coherent extreme ultraviolet radiation from the phenomenon of high-order harmonic generation. He is also interested in the intense THz generation methods and THz time-domain spectroscopic applications.

Tsuneyuki Ozaki graduated from University of Tokyo, Japan in 1987, where he also received his M.Sc. and Ph.D. degrees in 1989 and 1998, respectively. From 1990 to 2000, he was a Research Associate at Institute for Solid State Physics, University of Tokyo, Japan. From 2000 to 2003, he was a Research Specialist at Nippon Telegraph and Telephone (NTT) Basic Research Laboratories, Atsugi, Japan. In 2003, he joined Institut National de la Recherche Scientifique (INRS), Varennes, QC, Canada, as an Assistant Professor. He is currently a Full Professor and the former Director of the Advanced Laser Light Source (ALLS) facility. His main research interests include high-intensity THz radiation sources and their applications, intense high-order harmonic generation, and the use of lasers in medicine. T. Ozaki has served on the Board of Directors of the International Committee on Ultra-high Intensity Lasers (ICUIL), and since 2018 is the Chair of Commission 17 on Laser Physics and Photonics of the International Union of Pure and Applied Physics (IUPAP).